Propagation and initiation mechanisms of the Madden-Julian oscillation

Kyong-Hwan Seo[1] and Kwang-Yul Kim

Department of Meteorology, Florida State University, Tallahassee, Florida, USA

Received 23 August 2002; revised 3 January 2003; accepted 25 March 2003; published 8 July 2003.

[1] An observational study of the propagation and onset mechanisms of the Madden-Julian oscillation (MJO) is performed using cyclostationary empirical orthogonal function analysis and a Kelvin-Rossby wave decomposition method for the NOAA outgoing longwave radiation and the NCEP/NCAR Reanalysis data. In these analyses, two different regions of surface convergence are observed ahead of MJO convection by different wind components as previously found in a SST-coupled GCM simulation. At the leading edge of enhanced convection, the friction-induced meridional convergence appears during the developing phase when the enhanced convection is located over the Indian Ocean and the Maritime Continents. Another region of surface convergence is identified just east of an enhanced convection core, and this tends to pull the convective core to the east. The surface convergence is formed by zonal wind convergence, and Kelvin and Rossby waves both play a comparable role in the formation of the convergence zone. Therefore the frictional Kelvin-Rossby wave-CISK (conditional instability of the second kind) is regarded as a primary factor for the eastward propagation of the MJO. Over the western Indian Ocean, moistening in the boundary layer occurs ~2 weeks earlier than the beginning of a new MJO cycle. This moistening accompanies low-level convergence by encircling Kelvin waves which propagated from the region of enhanced convection during the previous cycle, as well as by Rossby waves generated from the region of reduced convection over the Indian Ocean. This earlier formation of the boundary-layer moisture convergence provides a favorable environment for triggering new convection. This interaction of Kelvin and Rossby waves also accounts for the suppression of convection from the western side of the convection core. For example, over the Indian Ocean, anomalous surface divergence appears at the western edge of the enhanced convection due to both circumnavigating Kelvin waves from the region of reduced convection of the previous cycle and Rossby waves from the region of the enhanced convection itself. Thus the MJO is a self-maintaining and self-generating form of tropical variability through the interaction between convection and large-scale circulation in the presence of boundary-layer dynamics. *INDEX TERMS:* 1620 Global Change: Climate dynamics (3309); 3309 Meteorology and Atmospheric Dynamics: Climatology (1620); 3374 Meteorology and Atmospheric Dynamics: Tropical meteorology; *KEYWORDS:* MJO, propagation of MJO, initiation of MJO

Citation: Seo, K.-H., and K.-Y. Kim, Propagation and initiation mechanisms of the Madden-Julian Oscillation, *J. Geophys. Res.*, *108*(D13), 4384, doi:10.1029/2002JD002876, 2003.

1. Introduction

[2] The Madden-Julian oscillation (MJO) is a dominant physical mode of the tropical intraseasonal variability [e.g., *Madden and Julian*, 1994]. It is characterized by an eastward propagating coherent global-scale tropical oscillation of a period of 30–60 days, having the prominent first baroclinic vertical mode. It has been detected in various meteorological and oceanic variables such as outgoing longwave radiation (OLR), precipitation, temperature, upper and lower tropospheric zonal winds, divergent and rotational wind fields [e.g., *Hsu*, 1996; *Chen and Chen*, 1997; *Matthews et al.*, 1999], sea level pressure (SLP) [e.g., *Matthews*, 2000], low-level moisture convergence [e.g., *Jones and Weare*, 1996], high-cloud coverage [*Zhang*, 1996], sea surface temperature (SST) [e.g., *Woolnough et al.*, 2000], and latent heat flux at the ocean surface [e.g., *Jones and Weare*, 1996; *Woolnough et al.*, 2000]. It is usually identified with a zonal dipole structure having the first two eigenvectors and principal component time series in out-of-phase relationships, respectively, from empirical orthogonal function (EOF) analyses [*Lau and Lau*, 1986; *Matthews*, 2000].

[1]Now at Climate Prediction Center, NOAA/NCEP, Camp Springs, Maryland, USA.

0148-0227/03/2002JD002876$09.00

[3] Other characteristics of the MJO are a 90° phase difference between the stream function and velocity potential [*Chen and Chen*, 1997], a modulation of the eastward propagating convective disturbance by an amplitude envelope with maxima over the Indian and western Pacific Oceans and a minimum over the Maritime Continents [*Zhang and Hendon*, 1997], and a geographical two-regime structure. The first regime is a convectively coupled wet regime with a zonal wave number-2 pattern over the equatorial warm pools. The second regime is a dry region with a zonal wave number-1 pattern at upper levels in the western hemisphere [e.g., *Madden and Julian*, 1972; *Bladé and Hartmann*, 1993].

[4] Although it is appreciated that perturbation available potential energy associated with latent heating in deep cumulus convection is the main energy source for the maintenance of the low-frequency, large-scale systems [e.g., *Yanai et al.*, 2000], essential aspects of the tropical intraseasonal oscillation, such as initiation and propagation mechanisms, still remain controversial. Also, a reason for the 30- to 60-day quasiperiodicity of the tropical oscillation is not clearly known. As a propagation mechanism, the wave-CISK (conditional instability of the second kind) theory proposes that deep cumulus convection induced by low-level moisture convergence forces eastward propagating Kelvin waves through the latent heat release, and the unstable waves induce low-level moisture convergence to the east of the original region of cumulus convection. In this way, the unstable waves pull the deep convection successively to the east. It was revealed, however, that the timescale of the oscillation by these dry eastward propagating equatorial Kelvin waves is too short to be comparable with observations. The introduction of cumulus friction [*Chang*, 1977], conditional heating (or positive-only heating) [*Lau and Peng*, 1987], and moist convection [e.g., *Emanuel*, 1987; *Neelin et al.*, 1987] in idealized models is shown to slow down the propagating speed of the convection anomaly closer to observations. However, most of the atmospheric general circulation models (AGCMs) simulate still shorter periods and weaker signals of the MJO than observations [e.g., *Lau and Lau*, 1986; *Slingo et al.*, 1996].

[5] These shortcomings tend to be overcome by introducing the boundary-layer frictional effect. Therefore the currently most prevailing paradigm, the frictional wave-CISK mechanism [e.g., *Wang and Rui*, 1990; *Wang and Li*, 1994; *Salby et al.*, 1994; *Hendon and Salby*, 1994, 1996; *Maloney and Hartmann*, 1998], is characterized by the eastward shift of frictionally driven boundary-layer moisture convergence relative to a convection center. Accordingly, meridional wind convergence also plays an important role in the mechanism. The frictional convergence of convectively driven surface winds appears 20°–40° east of a convection system and provides additional available potential energy through the convergence of moisture and subsequent latent heating, while the convectively driven convergence (divergence) in the lower (upper) troposphere appears in phase with the convective forcing.

[6] Alternative mechanisms are involved in the coupled air-sea interactions. *Emanuel* [1987] and *Neelin et al.* [1987] argue that surface easterly anomalies on the eastern side of a convective anomaly could enhance surface evaporation into the air under the presence of the easterly mean state, making the atmospheric boundary layer unstable enough to generate new convection. On the other hand, to the west of the convection, a westerly anomaly decreases total wind speed and induces surface evaporative cooling, thereby suppressing convection. This theory of wind-induced surface latent heat flux is now known to be somewhat misleading due to the existence of mean westerlies over the warm-pool region.

[7] Recently, the role of sea surface temperature (SST) for the maintenance and development of the MJO has received growing interest. A theoretical work by *Wang and Xie* [1998] shows that the ocean mixed layer thermodynamic processes tend to destabilize the MJO and provide its longwave selection mechanism. Diagnostic analyses [e.g., *Shinoda et al.*, 1998; *Woolnough et al.*, 2000] also suggest the importance of the air-sea coupling processes. It is found that to the west of a convection anomaly, a surface westerly anomaly reinforces total wind in the presence of time-mean westerlies over the warm pools and leads to enhanced oceanic vertical mixing and evaporation into the atmosphere. Along with these, reduced downward shortwave radiation fluxes due to the shielding effect of deep cloud systems tend to decrease the underlying SSTs. To the east of a convection anomaly, the situation is reversed; there appears a positive SST anomaly. A composite study of *Kemball-Cook and Wang* [2001] presents a dominant mechanism similar to the above for the northward propagation of boreal summer intraseasonal oscillation. A general circulation model (GCM) simulation with SST coupling results in a slowdown of the migrating speed of the MJO closer to observations, more organized convective cells, and improved seasonality through the interaction with the surface latent heat and shortwave fluxes generated by the MJO [e.g., *Flatau et al.*, 1997; *Waliser et al.*, 1999; *Woolnough et al.*, 2001; *Hendon*, 2000; *Kemball-Cook et al.*, 2002]. Especially, the results of the incorporation of prognostic SST anomalies to a GCM by *Waliser et al.* [1999] suggest that both the frictional wave-CISK by meridional winds at the east of the MJO convection and zonal wind convergence just ahead of the MJO convection center are important for the maintenance of the MJO.

[8] Theories on the initial development process of MJO convection can be classified as internal (tropical) and external (extratropical) triggering mechanisms. In the tropics, a previous cycle of the MJO can initiate new convection over Africa or over the western Indian Ocean. This internal tropical triggering theory is associated with wave-CISK or frictional wave-CISK, and large-scale circulation anomalies encircling the tropics are responsible for the initiation of a new convective cycle [e.g., *Hendon*, 1988; *Bladé and Hartmann*, 1993; *Matthews*, 2000; *Yanai et al.*, 2000]. Because the main agent is Kelvin waves of the upper or lower level wind or its divergence induced by a previous convection anomaly, there is no need for convection anomalies to be existent in the western hemisphere.

[9] As another internal triggering mechanism, a discharge-recharge theory by *Bladé and Hartmann* [1993] in their two-level global nonlinear model study suggests that the local oscillation of discharge and recharge of convective instability determines the initiation and period of the oscillation. A similar line of conjecture is made by *Hendon and*

Liebmann [1990] for the intraseasonal oscillation of the Australian summer monsoon. Recent composite studies of the low-level moist static energy using tropical radiosonde data [*Kemball-Cook and Weare*, 2001] and of the NASA Water Vapor Project water vapor integrated from the surface to 300 hPa [*Maloney and Hartmann*, 1998] support this theory to some extent.

[10] Extratropical triggering theory suggests that extratropical Rossby wave propagation or energy dispersion from midlatitude baroclinic eddies into the tropical Indian Ocean [e.g., *Hsu et al.*, 1990; *Bladé and Hartmann*, 1993; *Slingo*, 1998; *Matthews and Kiladis*, 1999; *Lin et al.*, 2000] initiates a following cycle of the MJO. As pointed out by *Kemball-Cook and Weare* [2001], however, there appears little indication of extratropical initiation by the intrusion of Rossby wave trains into the Indian Ocean in the upper level circulation.

[11] The role played by equatorial Kelvin and Rossby waves induced by the tropical heating has been investigated by several authors. Although a theoretical analysis of *Wang and Rui* [1990] expects moist Kelvin waves to emerge but Rossby waves to decay for high SST, observational and GCM studies [e.g., *Lau et al.*, 1989; *Sperber et al.*, 1997; *Matthews et al.*, 1999; *Matthews*, 2000] show the existence of the response of Rossby waves. The Gill-type response structure [*Gill*, 1980] serves to provide insights into the behavior of these waves. For example, the eastern response for equatorial diabatic heating corresponds to the circulation of Kelvin waves and the western part reveals a Rossby wave pattern with a symmetric off-equator cyclone or anticyclone pairs [*Lau et al.*, 1989; *Matthews*, 2000]. However, large-scale circulation anomalies generated by a pair of MJO enhanced convection and reduced convection may complicate the pattern so that sometimes it is difficult to interpret the exact manner in which Kelvin and Rossby waves propagate.

[12] *Matthews et al.* [1999] decompose the total equatorial divergence field into a zonal and meridional wind convergence, and view the equatorial zonal wind convergence as a Kelvin wave signature. As mentioned earlier, however, since much of the MJO life cycle is characterized by a traveling zonal dipole structure of the OLR anomaly field, the zonal wind near the Maritime Continents has a Rossby wave response by the eastern OLR anomaly as well as a Kelvin wave response by the western OLR anomaly. It is considered that the zonal wind convergence computed by the undecomposed zonal wind does not faithfully show a clean Kelvin wave signal, although this might provide a valid hint for Kelvin wave propagation.

[13] In this study, we investigate the propagation and initiation mechanisms of the MJO by examining surface convergence and Kelvin and Rossby wave propagation. This will also reveal the relative importance of Kelvin and Rossby waves in causing the oscillation, as well as in the interaction between convection anomalies of opposite sign via these waves. To address these problems, a clearer signal of the MJO should be obtained from observed data. For this, a new statistical technique called the cyclostationary empirical orthogonal function (CSEOF) method is introduced. It will be seen later that this method effectively isolates the repeated evolution of physical processes with a broad temporal band of variability.

[14] Furthermore, in an effort to separate Kelvin and Rossby wave responses, decomposition is made by projecting the Hermite functions on observational data in the meridional direction. This technique successfully extracts Kelvin or Rossby wave signals embedded in the noisy and asymmetric fields. As will be seen later, the equatorial zonal wind convergence by Rossby waves has a comparable magnitude to that by Kelvin waves, and the decomposed sea level pressure anomaly reveals a westward propagating Rossby wave over the dry region of the central and eastern Pacific.

[15] The spectral peak of the MJO is most pronounced during boreal winter and spring. To obtain a higher degree of symmetry about the equator and avoid the effect of the ENSO (El Niño and Southern Oscillation), and thus to infer possible mechanisms under a simpler atmospheric condition, only springtime tropical variability is considered in this study.

2. Data

[16] Two primary data sets are used in this study. First, a daily mean interpolated satellite derived OLR data set [*Liebmann and Smith*, 1996] on a 2.5° × 2.5° grid for the whole longitudes between 20°N and 20°S is used for a 22-year period from 1979 to 2000 as a proxy for deep tropical convection. Second, daily sea level pressure (SLP), specific humidity, and winds at the standard levels and 10 m are obtained from the National Centers for Environmental Prediction-National Center for Atmospheric Research (NCEP-NCAR) reanalysis data set [*Kalnay et al.*, 1996]. Zonal and meridional winds at 10 m have a Gaussian meridional grid and the others have a 2.5° × 2.5° spatial resolution. Only 22-year data from 1979 to 2000 are used in this study.

3. Methods of Analysis

3.1. Power Spectrum

[17] Seasonal cycle of each variable has been first removed and EOF principal component (PC) time series for each mode are bandpassed with the Parzen filter [*Newton*, 1988] to take only the 30- to 60-day signal. Using 100 such filtered modes, which account for more than 90% of the total variability, the fields were reconstructed. The temporal filtering in EOF space (i.e., filtering of PC time series) is equivalent to temporal filtering in physical space (i.e., filtering of time series at each station), and the former approach is more efficient. Because only springtime variability is taken into account in this study, a 96-day time series beginning from March 1 to June 4 is taken for each year. Thus the entire time series consists of 2112 days of data.

[18] Figure 1 shows the autoregressive (AR) spectral density function of the resulting time series along the equator between 40°E and 80°W. The best order of the AR model was determined objectively by the criterion autoregressive transfer function (CAT) [*Newton*, 1988]. As can be seen, significant power is in the band of the 30- to 60-day period, with a maximum around the 40-day period. The AR spectrum based on the entire record instead of the

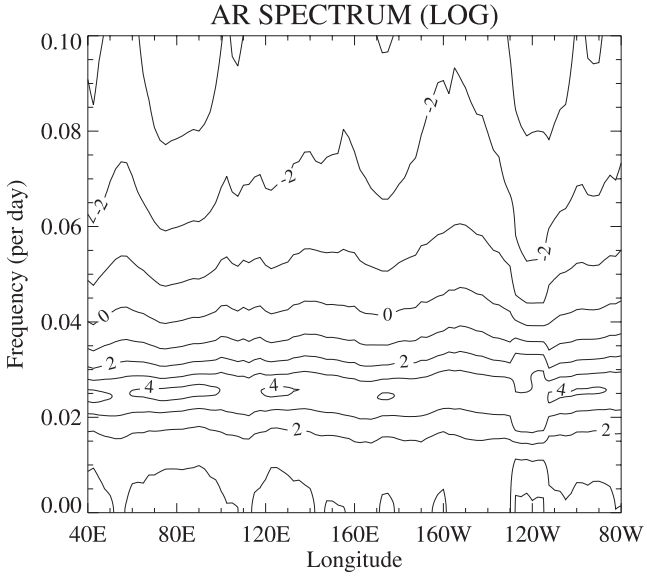

Figure 1. The AR spectral density function of the 30- to 60-day springtime OLR variability along the equator.

springtime record shows a similar band of significant power with a maximum around 48 days.

3.2. CSEOF Analysis

[19] To obtain recurrent patterns, a CSEOF technique [*Kim et al.*, 1996; *Kim and North*, 1997] is applied to the filtered data. In this method, space-time data are written as a linear combination of CSEOFs,

$$T(r,t) = \sum\nolimits_n LV_n(r,t)PC_n(t), \tag{1}$$

where $LV_n(\boldsymbol{r}, t)$ and $PC_n(t)$ are cyclostationary loading vectors and principal component (PC) time series. This representation of data is similar to but differs from the EOF expansion in that the loading vectors are time dependent and periodic, i.e.,

$$LV_n(r,t) = LV_n(r,t+d). \tag{2}$$

The loading vectors are dependent upon time because they are eigenfunctions of a space-time covariance function instead of only a space-dependent covariance function as in conventional EOF analysis. It is emphasized that the CSEOF loading vectors represent temporally evolving physical processes (say, the MJO) whereas the PC time series represent the amplitude modulation of the physical processes at longer timescales.

[20] The so-called nested periodicity, d, represents an inherent physical timescale and is chosen to be 48 days (see Appendix A). The nested period is slightly different from the period of the spectral peak in Figure 1. It should be noted, however, that the spectral peak is fairly wide, including appreciable amount of variability in the 30- to 60-day band. This may indicate that the physical period varies from one MJO event to another. The phase might also change from one MJO event to another. Thus the MJO should not be viewed as a process with a fixed physical period; as a result, such a physical process may not be represented as a single mode in the CSEOF analysis. As shown in Appendix B, a physical process with "disturbed" period and phase is represented as two modes in the CSEOF analysis. The two modes are identical except that they are 90° out of phase; the reasoning behind this is analogous to the following. Fourier transformation of $A\cos(\omega' t)$ results in both $\cos(\omega t)$ and $\sin(\omega t)$ components when the frequency ω' is slightly disturbed from ω. A similar result follows when the phase θ' is slightly disturbed from zero in $A\cos(\omega t + \theta')$. It certainly is not a good property of an analysis technique that a physical process is divided into two modes; bear in mind, however, that the MJO physical process is variable in nature.

[21] In a conventional approach such as EOF analysis or composite analysis, propagating or evolving patterns are extracted based on lag-correlation analysis. For example, the first two EOF PC time series are assumed to have an exactly 90° phase difference and the evolution pattern is determined by assuming sinusoidal variation of the two PCs [e.g., *Lau and Lau*, 1986; *Maloney and Hartmann*, 1998; *Matthews*, 2000]. The period of oscillation is typically determined by the lag of maximum correlation between the two PCs, while the period of the MJO, in practice, is known to fluctuate widely [*Matthews*, 2000]. Even when the period is allowed to vary, the evolution patterns of the MJO cycle do not change because they are constructed based on the addition of the first two EOFs. Thus the assumption of a nested period in CSEOF analysis does not introduce additional constraints over a conventional approach. On the other hand, the former approach avoids the assumption that two EOF patterns describe the physical evolution of the MJO. In fact, reconstructed data based on the first cyclostationary loading vector and the corresponding PC time series is decomposed into more than two EOFs, although the higher modes are much smaller than the first two EOF modes. CSEOFs are also compared with extended EOFs and complex EOFs and their corresponding PCs in Appendix C.

3.3. Regression Analysis

[22] CSEOFs are computed independently for individual variables so that resulting PC time series are generally different between two different variables. Hence, to obtain dynamically consistent patterns between two variables, a regression or projection method is required. For this, the resulting PC time series (predictor time series) is regressed onto the PC time series of the other variable (target time series) in the CSEOF domain. Namely, one needs only to find a set of regression coefficients, $\{a_n\}$, such that a residual error is minimized,

$$PCT_i(t) = \sum\nolimits_n a_n PC_n(t) + \varepsilon(t), \tag{3}$$

where $PCT_i(t)$ is the target PC time series for mode i, $PC_n(t)$ is the predictor time series for mode n, and $\varepsilon(t)$ is residual error. In this study the target variable is OLR and predictor variables are SLP and winds at 10 m. The degree of fitting for each mode is estimated by a determination coefficient, $r_i^2 = \langle \varepsilon^2(t) \rangle / \langle PCT_i^2(t) \rangle$, where the angle brackets denote ensemble averaging.

[23] Then the resulting spatial pattern of the predictor variable, $LVP_i(\boldsymbol{r}, t)$, being consistent with the pattern of the

target variable, is obtained by a linear combination of the cyclostationary eigenvectors of the predictor variable, $LV_n(\boldsymbol{r}, t)$, such that

$$LVP_i(r,t) = \sum\nolimits_n a_n LV_n(r,t). \tag{4}$$

In this practice, the first 10 PC time series of predictor variables are used (i.e., $n = 10$) to match the pattern of OLR. Since the first two modes for each predictor variable explain over 90% of the variability of the target PC (the first CSEOF PC of the OLR field), the inclusion of more modes in equation (4) does not significantly affect the overall pattern and magnitude.

3.4. Kelvin and Rossby Wave Decomposition

[24] The regressed fields of SLP and winds at 10 m are further decomposed into Kelvin and Rossby waves. This can be performed by solving the forced, viscid shallow-water equations as discussed in Appendix D. The main derivation is that solutions for the shallow water system can be expanded into Kelvin and Rossby waves in the long-wave approximation. These waves can be expressed by the Hermite polynomials in the meridional direction.

[25] Using normalized Hermite functions, $\Psi_n(y)$, the meridional structure functions (see Appendix D) of Kelvin wave for the zonal wind and SLP are written as

$$u_0 = \frac{1}{\sqrt{2}}\Psi_0(y), \qquad slp_0 = \frac{1}{\sqrt{2}}\Psi_0(y), \tag{5}$$

and those of the nth Rossby wave are

$$\begin{aligned} u_n &= \sqrt{\frac{n(n+1)}{2(2n+1)}}\left(\frac{\Psi_{n+1}}{\sqrt{n+1}} - \frac{\Psi_{n-1}}{\sqrt{n}}\right), \\ slp_n &= \sqrt{\frac{n(n+1)}{2(2n+1)}}\left(\frac{\Psi_{n+1}}{\sqrt{n+1}} + \frac{\Psi_{n-1}}{\sqrt{n}}\right). \end{aligned} \tag{6}$$

Thus the regressed SLP patterns are decomposed into

$$LVP_i(r,t) = \sum_{m=0}^{M} \alpha_m(x,t) slp_m(y), \tag{7}$$

where $\alpha_m(x, t)$ are expansion coefficients and can be found by solving a set of simultaneous equations using a singular value decomposition (SVD) algorithm [e.g., *Press et al.*, 1992].

4. Results

[26] In this section, we present the CSEOFs of OLR and the regressed patterns of other variables. As described above, CSEOF analysis has been conducted on all variables considered in this study. Then, regression analysis has been carried out on all variables except for OLR to find spatial patterns of physical variables consistent with those of OLR (e.g., see Figure 3 in section 4.1).

4.1. Life Cycle of Tropical Convection

[27] Figure 2 is the longitude-time plot of the first six CSEOFs, weighted by the respective standard deviation, of the OLR field along the equator. They explain, respectively, 20, 17, 9, 6, 5, and 4% of the total variability. The first two modes clearly show the eastward propagating OLR variability. The other modes do not show any significant eastward propagating signals. In this study, we will inves-

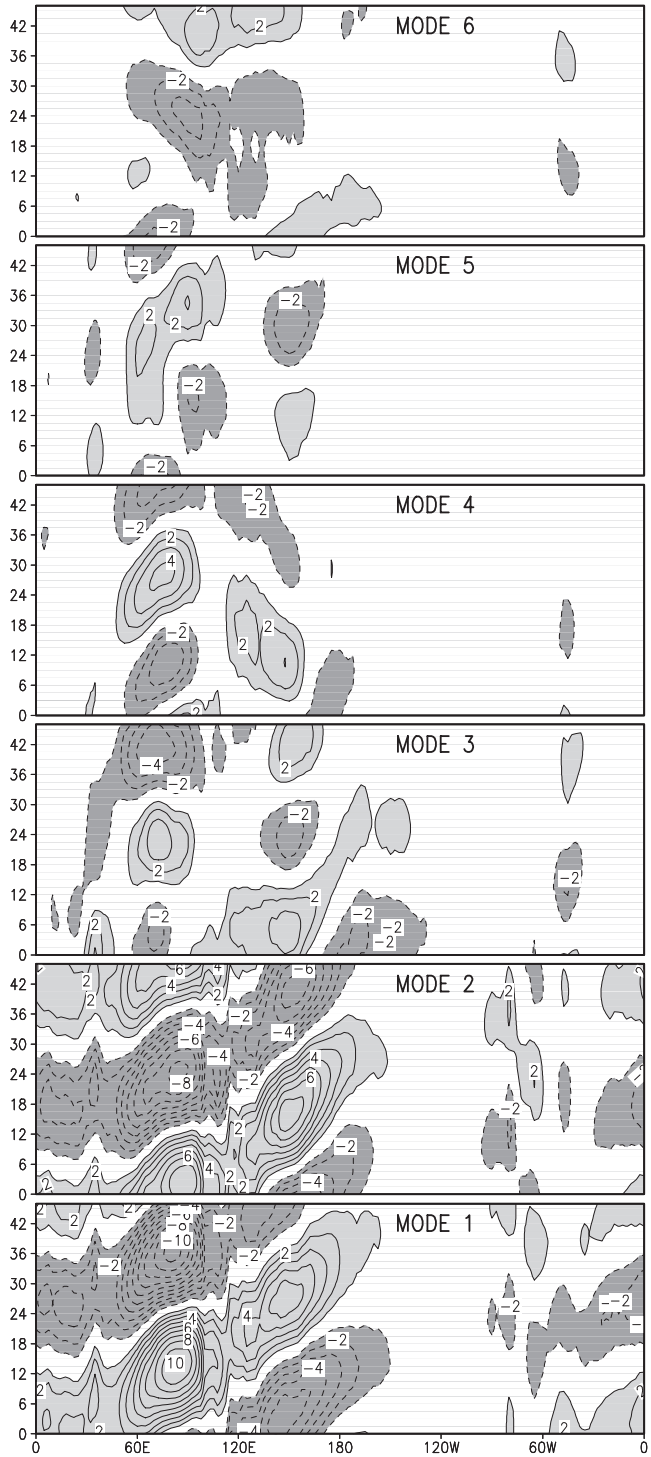

Figure 2. The longitude-time plot of the first six CSEOFs of the OLR field (Wm^{-2}) along the equator. The CSEOFs are weighted according to the standard deviation of the respective PC time series.

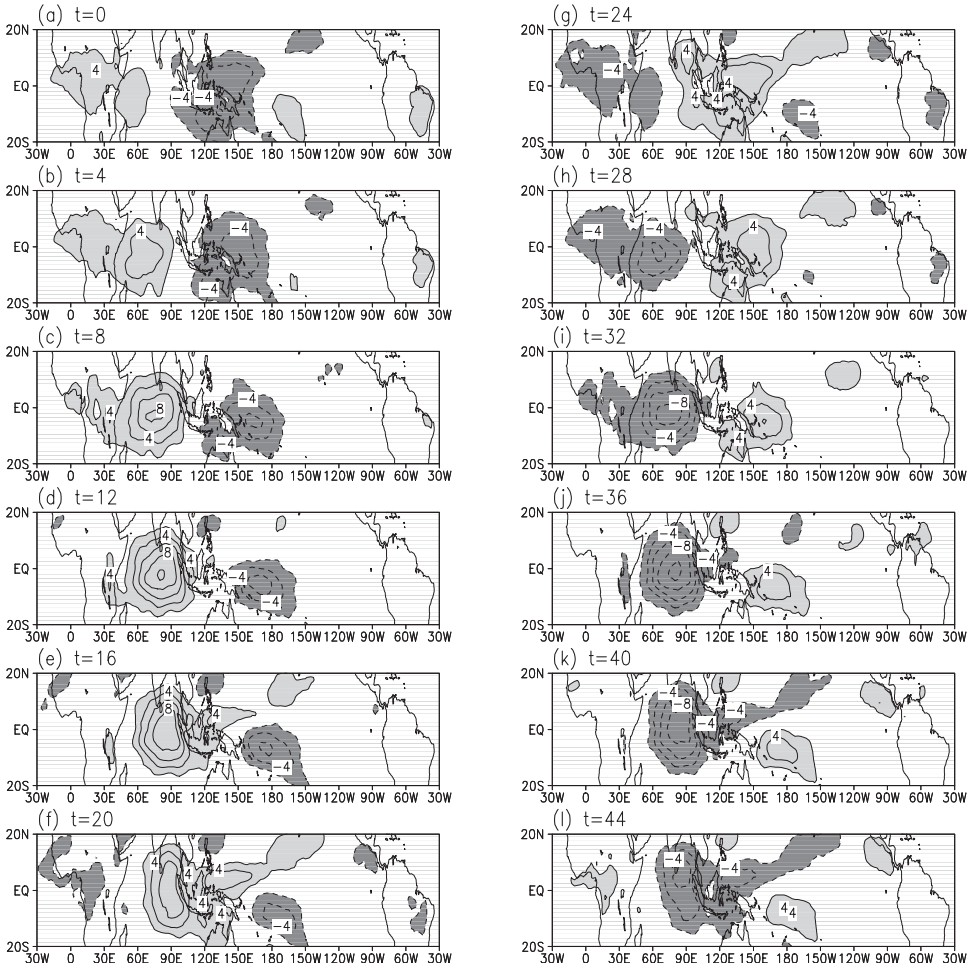

Figure 3. Time evolution of the first CSEOF mode of OLR anomalies at intervals of 4 days. Negative (positive) OLR anomaly is shaded heavily (lightly). Contour interval is 2 Wm^{-2}.

tigate only the eastward propagating component of the OLR field and the associated dynamical response of the atmosphere. The eastward propagating signals do not have exactly the 48-day period; the period and the phase of the events appear to change from one event to another in the filtered data. As discussed earlier, a period-varying signal is decomposed into two modes, and they have a 90° out-of-phase relationship in the CSEOF method. A prior test using simpler cases designed to mimic the MJO propagation illustrates the way the non-phase-locked oscillation is handled in the CSEOF method (see Appendix B). We only consider the first mode, since the second mode essentially depicts the same physical evolution of the OLR field. The first two PC time series are shown in Figure C3 in Appendix C.

[28] The temporal evolution of the convection anomalies for the first mode is shown in Figure 3. It is seen that new enhanced convection begins to develop in the tropical region of Africa at $t = 20$. Over the western Indian Ocean, an enhanced convection event occurs and intensifies after $t = 20$. The convection anomaly over Africa weakens and disappears at $t = 40$; meanwhile, it attains its maximum intensity at $t = 36$ over the Indian Ocean. During its passage over the Maritime Continents, the convection anomaly becomes weaker ($t = 44$, 0, and 4). Over the west Pacific, it develops again ($t = 8$) and decays ($t = 20$) as it moves off eastward toward the date line.

4.2. Vertical Propagation of Zonal Wind

[29] Figure 4 shows the time sequence of the vertical structure of the zonal wind at (130°E, 0°N) associated with the first CSEOF of the OLR field. A first baroclinic structure is clearly seen with amplitude peaks around 600–800 hPa and 100–150 hPa. The internal waves exhibit a peculiar vertical propagation. Propagation is upward in the lower troposphere and downward in the upper troposphere and lower stratosphere. The equatorial Kelvin and the first Rossby components of the zonal wind (Figures 4b and 4c) also have the same phase propagation property. This observation is consistent with the energy flux, since many types of internal waves in the atmosphere exhibit a phase propagation opposite to the propagation of wave group (energy). The wave energy generated by convective heating centered around 300–500 hPa radiates upward in the upper troposphere and downward in the lower troposphere [e.g., *Chen and Yanai*, 2000; *Yanai et al.*, 2000]. Indeed, the smaller propagation speed in the lower troposphere compared with that in the upper atmosphere is a reflection of the smaller

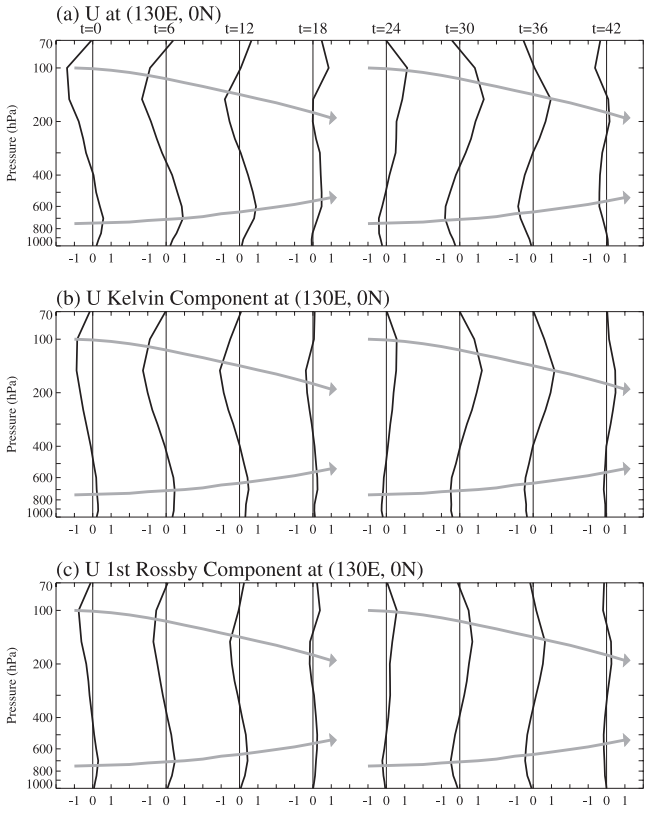

Figure 4. Time sequence of the vertical structure of (a) the zonal wind anomaly, (b) the Kelvin component of the zonal wind anomaly, and (c) the first Rossby component of the zonal wind at (130°E, 0°N) associated with the first CSEOF of the OLR field.

vertical flux of wave energy in the lower troposphere shown by *Yanai et al.* [2000, Figure 13].

4.3. Frictional Convergence in the Boundary Layer

[30] To investigate the development and propagation mechanisms of the MJO, surface horizontal convergence and Kelvin-Rossby wave responses are taken into account. Figure 5 shows the SLP and the near-surface wind convergence at the growing stage of the enhanced convection over the Indian Ocean (t = 34 in Figure 3). The negative SLP anomaly well matches with the enhanced convection anomaly (Figure 5a). The leading edge of the negative SLP anomaly goes beyond the enhanced convection anomaly into the region of reduced convection anomaly. To the west of the main core of the enhanced anomaly, on the other hand, the positive SLP anomaly appears with its shape resembling the Kelvin wave intrusion.

[31] Figure 5b shows the wind and its horizontal convergence at 10 m. The westerlies (easterlies) appear to the west (east) of the enhanced convection. The easterlies are much stronger than the westerlies; this is attributable to the combined effect of Kelvin and Rossby waves due to the dipole structure of the convection anomalies over the Indian and the Pacific Oceans (see Figure 6). A careful look reveals that the direction of the zonal wind changes around 85°E, which is east of the convection center located at ~75°E. Therefore a convergence region is formed just east of the enhanced convection core. In contrast, convergence or divergence at 850- and 200-hPa levels, although the plots are not presented for brevity, is in phase with the core of the convection anomaly as shown by *Hendon and Salby* [1994]. This circulation pattern in the free troposphere is qualitatively consistent with the heat-generated anomalous circulation of the Gill type.

[32] Moreover, another convergence region appears at the leading edge of the enhanced convection. This helps generate a new convection cell as manifested in the small bulge of the negative OLR anomaly at the eastern edge. It appears that these two convergence regions are formed by different wind components. Right downstream of the enhanced convection core, the convergence is mainly from the zonal wind component (Figure 5c), whereas the convergence region further east is mainly due to the meridional wind (Figure 5d). The meridional convergence at the leading edge of the enhanced convection seems to be caused by the boundary layer friction (a more complete picture of which will be presented later). The convergence at the leading edge of the enhanced convection anomaly leads to the generation of a new convection cell, whereas the convergence just east of the convection center appears to be more associated with an eastward movement of the entire super cloud clusters. Considering the fact that the boundary layer is very moist, this "lead" of the convergence regions with respect to the center of the convection anomaly can be considered as a main propagation mechanism of the MJO. A further analysis is performed to investigate the formation of this convergence by exploring the relative role of Kelvin and Rossby waves of zonal wind. A significance test has been conducted by calculating correlation of filtered SLP and zonal and meridional wind convergence at each sampling station with the CSEOF PC time series of OLR (see Appendix C). The resulting correlation maps indicate that the gross features of the regressed patterns are captured at the 95% confidence level (not shown). Therefore the convergence identified in Figure 5 is by no means negligible and the following Kelvin and Rossby waves are regarded statistically significant.

[33] Figure 6 shows the Kelvin and Rossby wave responses of the zonal wind and their respective convergences. The shaded region of the zonal winds in Figures 6a and 6c appears to show that the Kelvin wave structure is broader than the first Rossby wave structure. This is because zonal wind changes sign at around ±20° in the first Rossby wave structure whereas the Kelvin wave structure extends much farther poleward (see Appendix D). As expected, easterly Kelvin waves for the zonal wind largely appear on the eastern side of the enhanced convection (Figure 6a). These waves are continuously generated and propagate eastward, while convection anomaly over the Indian Ocean develops and propagates to the east. The Rossby wave response to the enhanced convection appears to be significantly weak on the western side of the enhanced convection (Figure 6c), whereas that on the eastern side of the enhanced convection has a comparable magnitude to the Kelvin wave response. Actually, this portion of the Rossby waves is developed as a response to the reduced convection over the west Pacific. The associated zonal wind convergence maximum is evident just ahead of the enhanced convection center, not only for the Kelvin waves (Figure 6b)

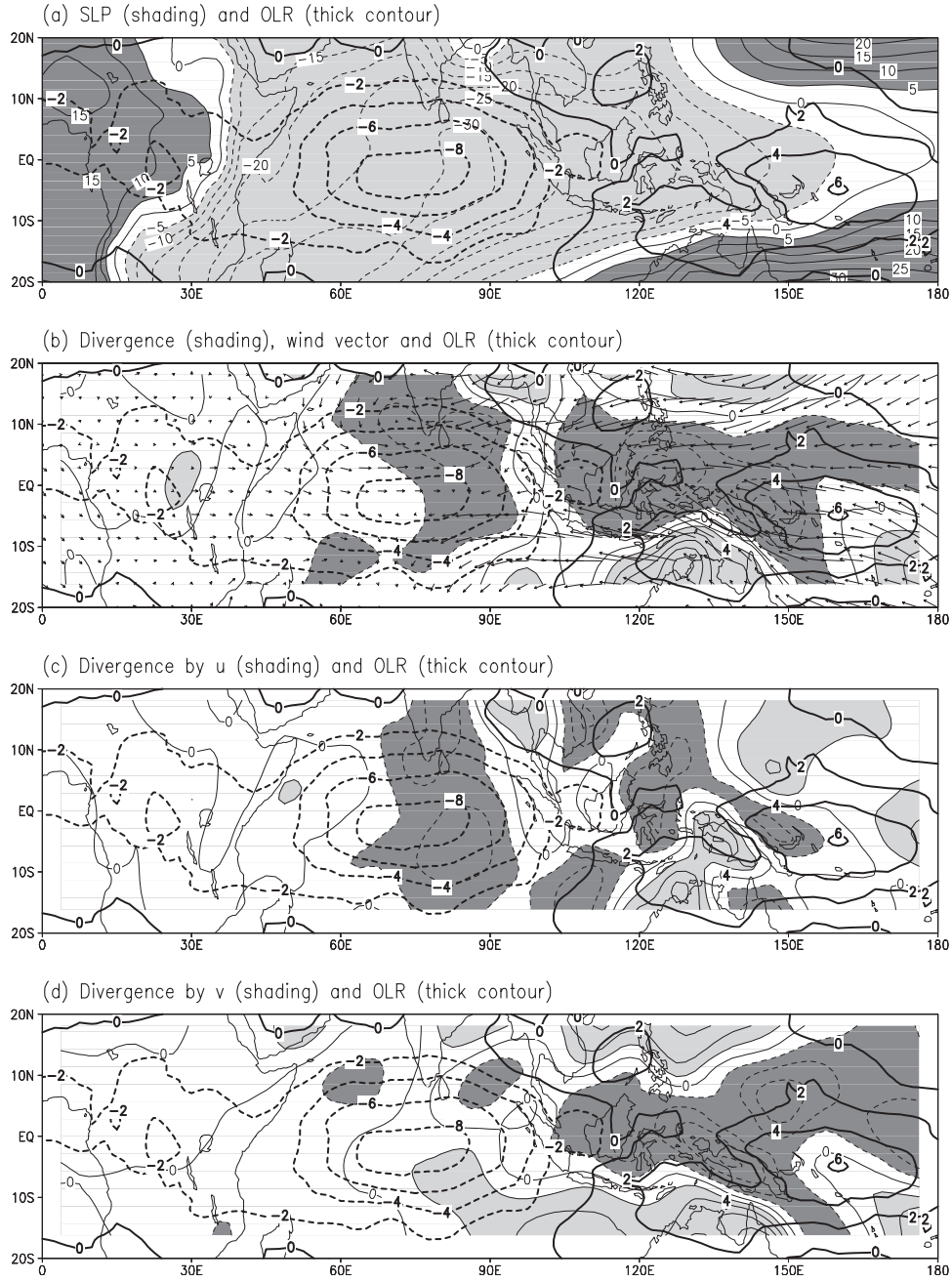

Figure 5. (a) Sea level pressure (thin lines and shading), (b) horizontal wind vectors and divergence at 10 m, (c) zonal wind divergence at 10 m, and (d) meridional wind convergence at 10 m at t = 34 day. OLR anomalies are superimposed as thick solid and dotted lines. Convergence (divergence) is shaded heavily (lightly). Contour intervals of SLP, divergence, and OLR anomalies are 5 Pa, 0.5×10^{-7} s^{-1}, and 2 Wm^{-2}, respectively.

but also for the Rossby waves (Figure 6d). This indicates again that the convergence in the eastern side of the enhanced convection (Figure 6a) is attributable to Kelvin waves produced by the enhanced convection over the central Indian Ocean, as well as Rossby waves by the reduced convection over the west Pacific. In other regions, downstream of the Indian convection core, Kelvin and Rossby waves induce the opposite sign of zonal convergence nearly canceling out each other. It appears that both Kelvin and Rossby waves cooperate for the downstream development of the moist convection, and in this way they foster the eastward propagation of the MJO signal.

[34] The SLP and the wind anomalies for the decaying stage of the enhanced convection (t = 6) are shown in Figure 7. The positive SLP anomaly begins to intrude onto the western edge of the enhanced convection. At this phase, the westerlies are widespread over the Indian Ocean and the west Pacific. In contrast, the easterlies appear only in the western hemisphere. Along the tropical region of the eastern hemisphere, anomalous surface divergence is dominant; the

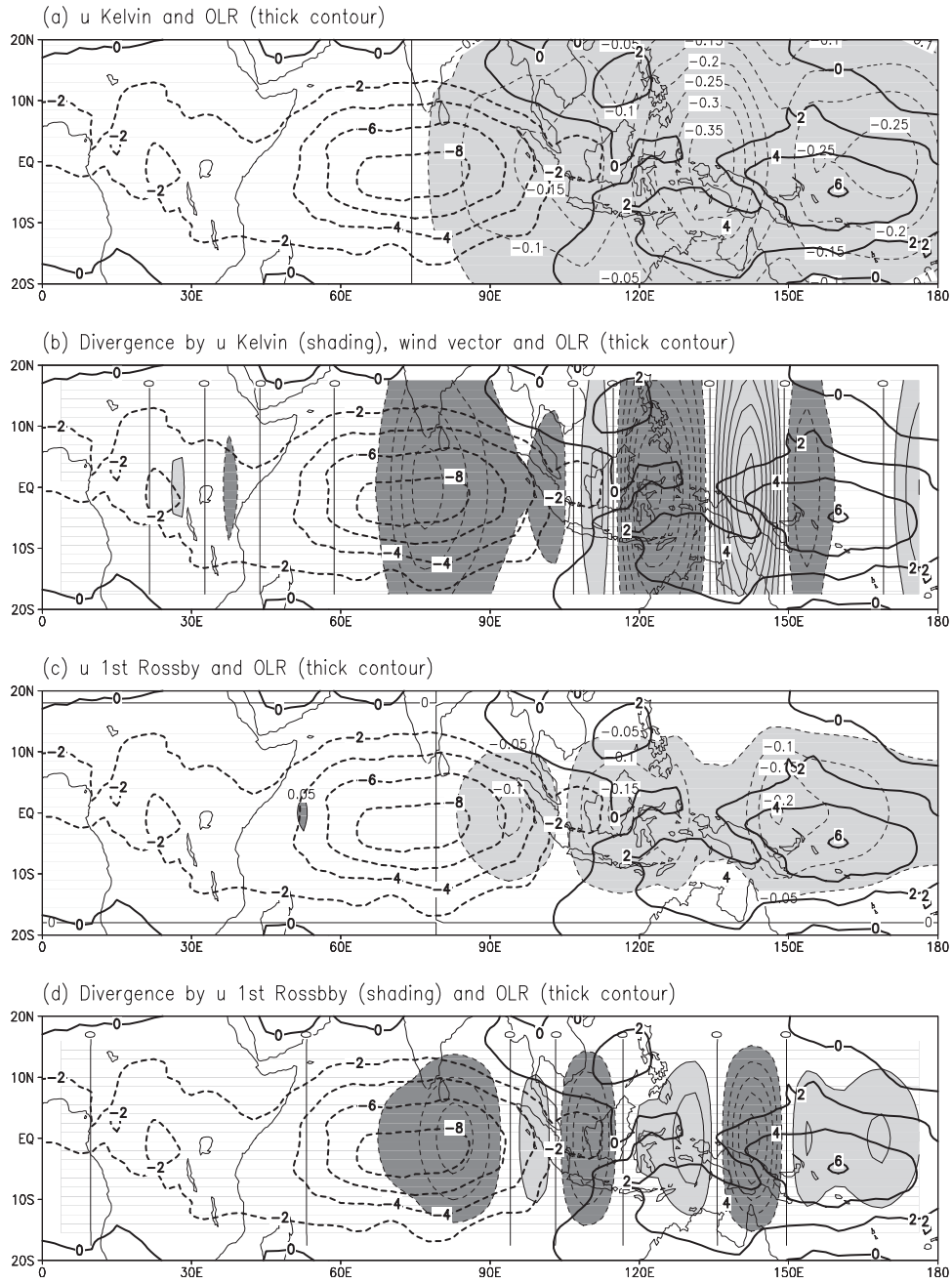

Figure 6. (a) Kelvin wave response of the zonal wind, (b) zonal wind divergence by Kelvin waves, (c) first Rossby wave response of the zonal wind, (d) zonal wind divergence by the first Rossby waves at $t = 34$ day. OLR anomalies are superimposed as thick solid and dotted lines. Convergence (divergence) is shaded heavily (lightly). Contour intervals of zonal wind, divergence, and OLR anomalies are 0.05 ms^{-1}, 0.5×10^{-7} s^{-1}, and 2 Wm^{-2}, respectively.

surface divergence appears even in the region of enhanced convection over the west Pacific. The leading edge of the enhanced convection shows a region of zonal wind convergence (Figure 7c), but meridional wind divergence (Figure 7d) offsets this so that the further development and maintenance of the enhanced convection is prohibited. Meridional wind convergence appears off the equator as a Rossby wave response.

[35] The meridional convergence (divergence) at the leading head of MJO enhanced (reduced) convection consistently appears during the movement of MJO convection over the warm pools in a similar manner to that shown in Figure 5d. This can be seen in Figure 8, which displays the meridional divergence along the zero OLR contours for enhanced (solid line) and reduced (dotted line) phases of MJO convection. The center of the MJO convection is located $\sim 30^\circ - 90^\circ$ to the west of the boundary of the two opposite convection anomalies. For enhanced (reduced) convection, meridional convergence (divergence) is strong mostly over the Indian and western Pacific Oceans. The

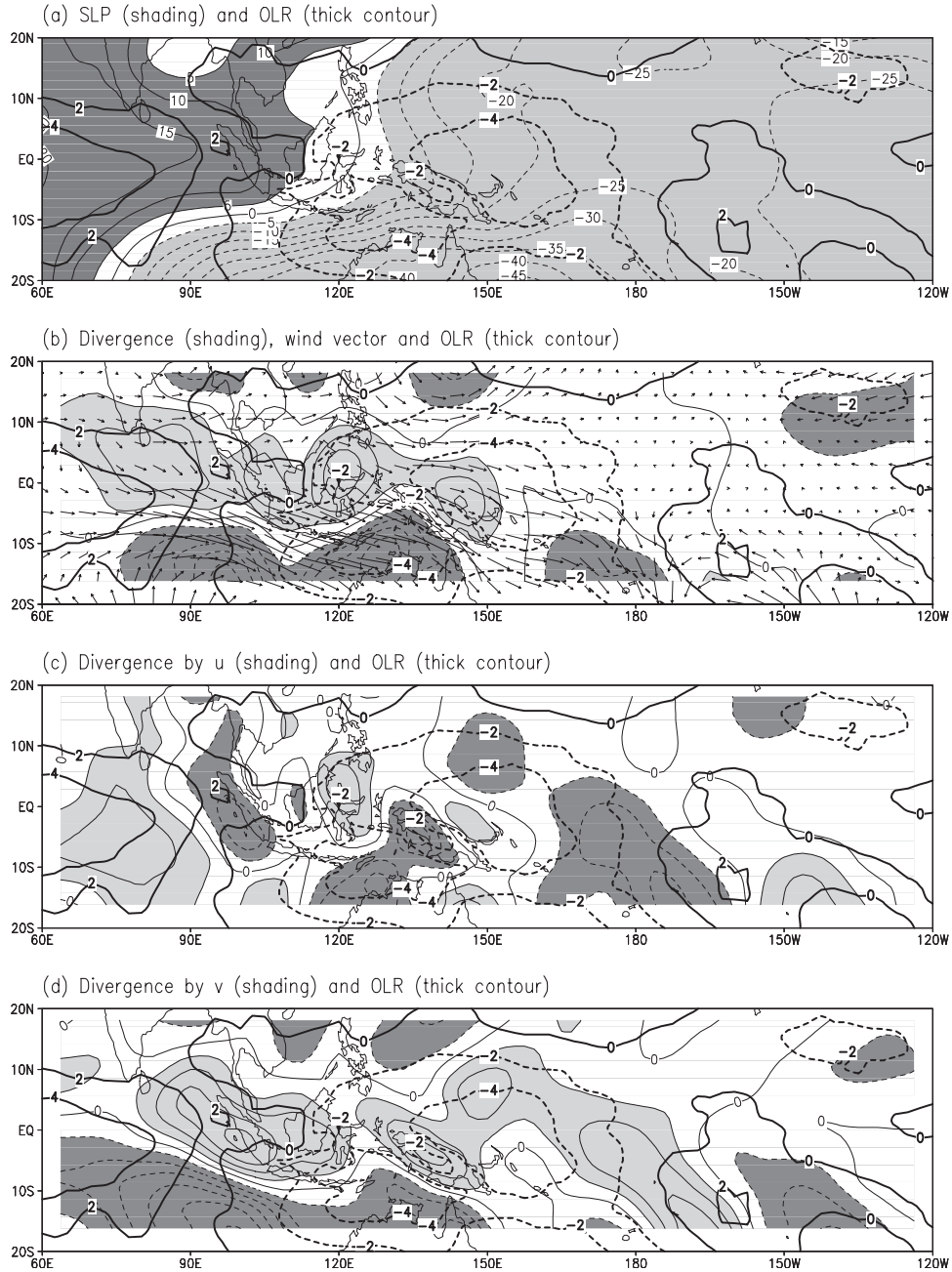

Figure 7. As in Figure 5 except for at t = 6 day.

strongest frictional convergence (divergence) appears during the developing phase when the enhanced (reduced) convection is located over the Indian Ocean at $t = \sim 32$ ($t = \sim 8$) (see Figure 3). After the center of convection moves to the east of $\sim 150^{\circ}$E (e.g., $t = \sim 8$ onward for enhanced convection), the convergence or divergence at the leading head of MJO convection significantly decreases, so there is no further support from the boundary layer for the growth of the MJO convection. This characteristic is an important factor for maintaining the MJO convection and is consistent with the frictional wave-CISK as given by *Hendon and Salby* [1994] and *Maloney and Hartmann* [1998].

[36] Along with this, there appears zonal wind convergence right at the downstream of the MJO center, which is found in the SST-coupled GCM simulation of *Waliser et al.* [1999]. The eastward movement of the entire MJO convection system is more directly associated with the formation of the zonal convergence. The propagation of the MJO will be investigated by examining Kelvin and Rossby waves of zonal winds. Figure 9 shows zonal wind divergence by Kelvin waves (Figure 9a) and Rossby waves (Figure 9b) with time. Comparing the phase propagation lines of OLR and divergence along their maxima and minima, after convection anomalies develop, the region of zonal wind convergence is found $\sim 30^{\circ}$ ahead of the center of the convection anomalies by the Kelvin wave response. The Rossby wave-induced convergence, which is comparable to the Kelvin wave-induced convergence, also appears down-

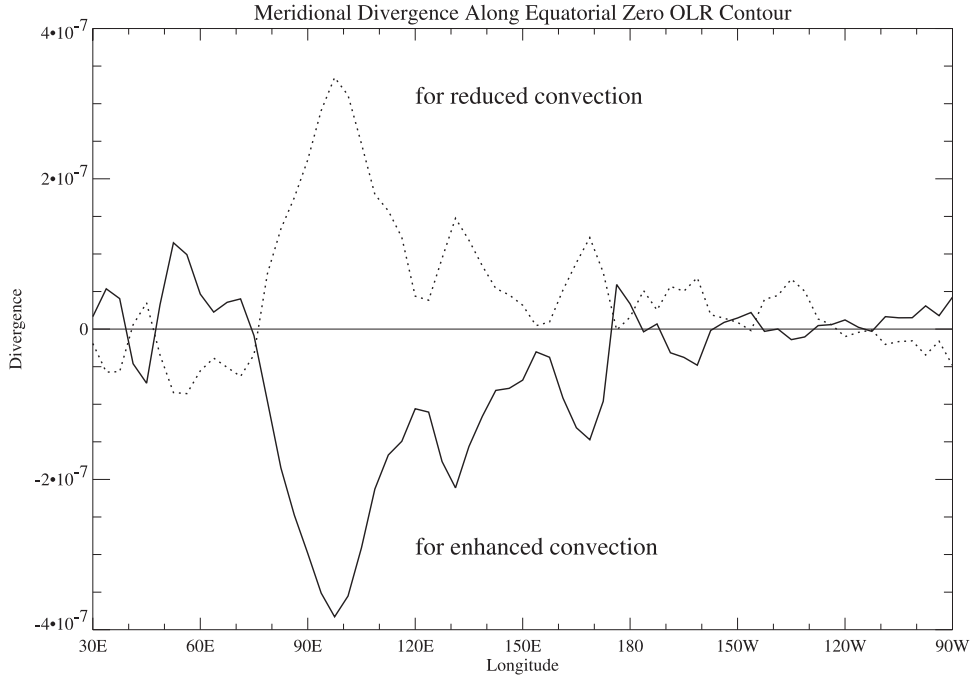

Figure 8. Equatorial divergence by meridional winds along the downstream zero OLR contours for enhanced convection (solid line) and reduced convection (dotted line). The divergence is averaged over a 7.5° × 10° longitude-latitude domain. Note that the core of the MJO convection is located ∼30°–90° to the west of the zero OLR contours.

stream of the enhanced convection (or upstream of the reduced convection), particularly over the Indian Ocean. This again implies that both Kelvin and Rossby waves contribute to the formation of the downstream convergence, which is the most important factor for the eastward propagation of the oscillation.

[37] In contrast, anomalous surface divergence appears at the western edge of the enhanced convection, particularly, over the Indian Ocean (∼50°E), after the convection anomalies sufficiently developed (i.e., t = 36 − 46), for both wave responses. Meridional wind convergence in these regions is much smaller than the zonal divergence (not shown). Therefore both waves act to suppress the enhanced convection from the western side. Note that a previous mechanism by *Matthews* [2000] suggests that the convection anomalies themselves are eroded by only their equatorial Rossby wave response. The divergence by Rossby waves is formed by the decrease in magnitude of the westerly anomalies from the enhanced convection core to the west. The divergence by Kelvin waves, however, involves an interaction between convection anomalies of opposite sign, which will be described in the next section.

4.4. Interaction and Initiation of the MJO Cycle

[38] In this section, an interaction between convection anomalies of opposite sign and a possible process for initiating a new MJO cycle will be investigated through wave propagation and moisture distribution. Figure 10 shows the Hovmöller diagram of Kelvin and first Rossby waves for the SLP anomalies (shadings) averaged from 5°S to 5°N. First, notice the two regions of discontinuity in the SLP propagation: near 35°E and 75°W. These represent the blocking of wave propagation by topographic barriers as also noted by *Matthews et al.* [1999] and *Matthews* [2000]. Also evident is that the Kelvin waves propagate largely at two different speeds. In the region where relatively strong OLR anomalies exist, the Kelvin waves propagate in conjunction with convection anomalies, moving as slow Kelvin waves [*Matthews et al.*, 1999]. This can be seen as a steep slope over the warm pools. In contrast, over the central and eastern Pacific Oceans, fast Kelvin waves are observed, since wave propagation is not coupled with convection in this region. Fast Kelvin waves are a manifestation of dry, freely radiating waves.

[39] It should be noted that Kelvin waves of the negative SLP anomaly arrive at the east Africa about 2 weeks before the enhanced anomaly begins to form there (t = ∼6). The negative SLP anomaly propagated from the enhanced convection region over the Indian Ocean at time t = −20 (i.e., previous cycle) and from the enhanced convection over the west Pacific at time t = 0. Thus, in Figure 9, the zonal divergence by the Kelvin component over the Indian Ocean at t = 36 − 46 is created by the encircling Kelvin waves forced by the reduced convection of the previous cycle over the Indian Ocean. Figure 10a also shows that the Kelvin waves of negative (positive) SLP anomaly generated by the enhanced (reduced) convection over the Indian Ocean propagate into the region of the reduced (enhanced) convection over the west Pacific at t = ∼26 (t = ∼2), tending to suppress the further development of the downstream reduced (enhanced) convection over the west Pacific. This counteracting effect on the downstream convection anomaly partly explains the asymmetry in the strength of the MJO convection over the Indian and west Pacific Oceans.

[40] The first Rossby wave response appears 30°–50° west of each convection anomaly. The Rossby wave group

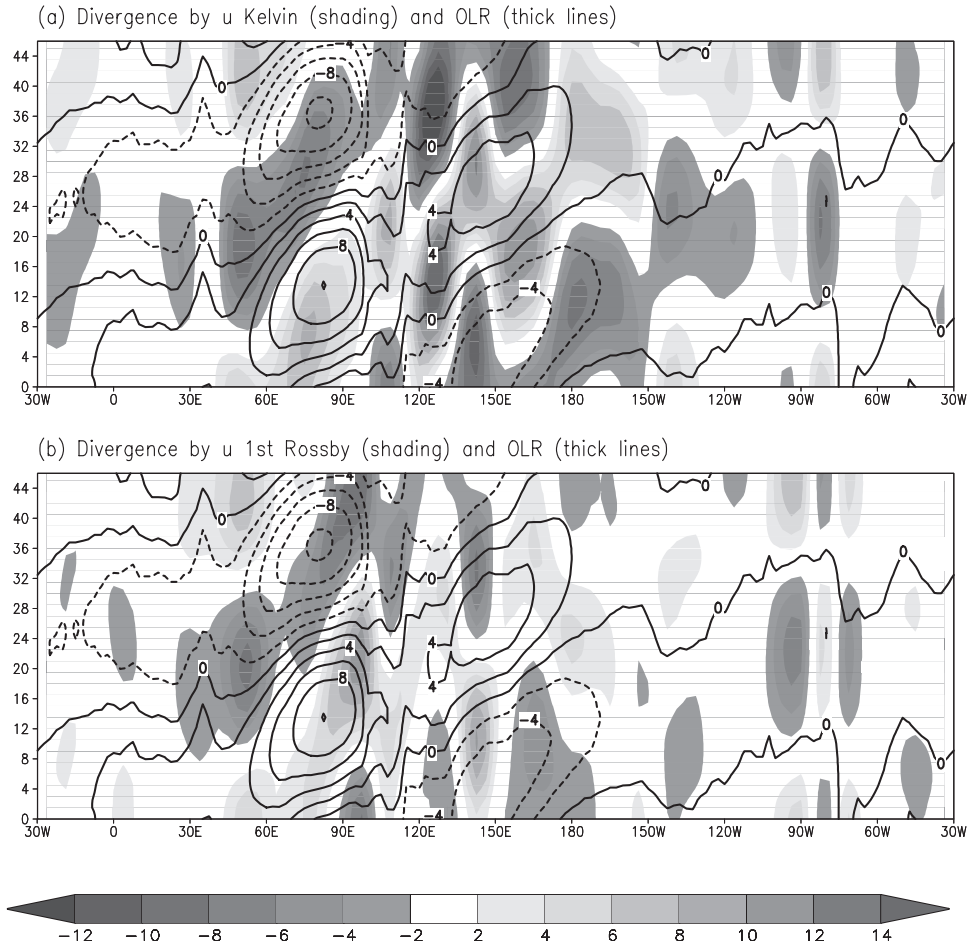

Figure 9. Hovmöller diagrams of zonal divergence (a) by Kelvin waves of the zonal wind anomaly (shading) and (b) by the first Rossby waves of the zonal wind anomaly (shading). Thick lines represent OLR anomalies with contour interval of 2 Wm^{-2}. Zonal wind convergence is in units of 10^{-8} s^{-1} with convergence (divergence) being shaded heavily (lightly). All quantities are averaged between 5°S and 5°N. Note that convergence (dark shading) appears east of the center of enhanced convection for both wave responses.

is also propagating eastward along with a moving convection anomaly as a forced response. As convective forcing decreases near the date line, however, the Rossby waves behave as free waves, showing a westward propagation (i.e., negative slope) over the eastern Pacific Ocean. Over the region between 30°W and 10°E, the wave group is also propagating westward. This disparate behavior of Rossby wave propagation makes it feasible to identify regions of a convectively coupled or uncoupled circulation, namely, forced or free waves.

[41] Figure 9 provides a hint of the importance of wave propagation during the onset process. It shows the formation of the convergence zone by both Kelvin waves (Figure 9a) and Rossby waves (Figure 9b) prior to the new convection over the western Indian Ocean (~50°E at t = 20). As seen earlier in the propagation of SLP (Figure 10a), the Kelvin waves propagated from enhanced convection over the Indian Ocean from the previous cycle (t = −20). The waves induce the surface convergence, which is a key element for triggering a new convection cell at t = 20. Also, the Rossby wave response forms the surface convergence over the western Indian Ocean at t = 12. The Rossby wave-induced convergence prior to the new cycle of the MJO is attributed to the reduced convection anomaly over the Indian Ocean. This convection anomaly affects the circulation to the west and induces the convergence after its peak phase.

[42] Figure 11 displays the vertical structure of the specific humidity anomaly as a function of time at the growing region of the convective disturbance. The time series of the tropical OLR anomaly is superimposed. It is seen that the reduced convection is characterized by the deep dry atmosphere, and the dry region lasts until one week after the negative OLR anomaly appears. During this phase of reduced convection, moistening appears in the lower layer starting about 2 weeks prior to the appearance of the negative OLR anomaly. The erosion of the dry region extends gradually upward until the enhanced convection begins to develop. After that, moistening takes place quickly in the middle and upper troposphere as seen in the steep slope of the positive specific humidity anomaly. This preappearance of moistening in the boundary layer builds up moist energy for the generation of new convection. This pattern of moistening has also been observed for the three MJO events during the TOGA COARE IOP [*Chen et al.*,

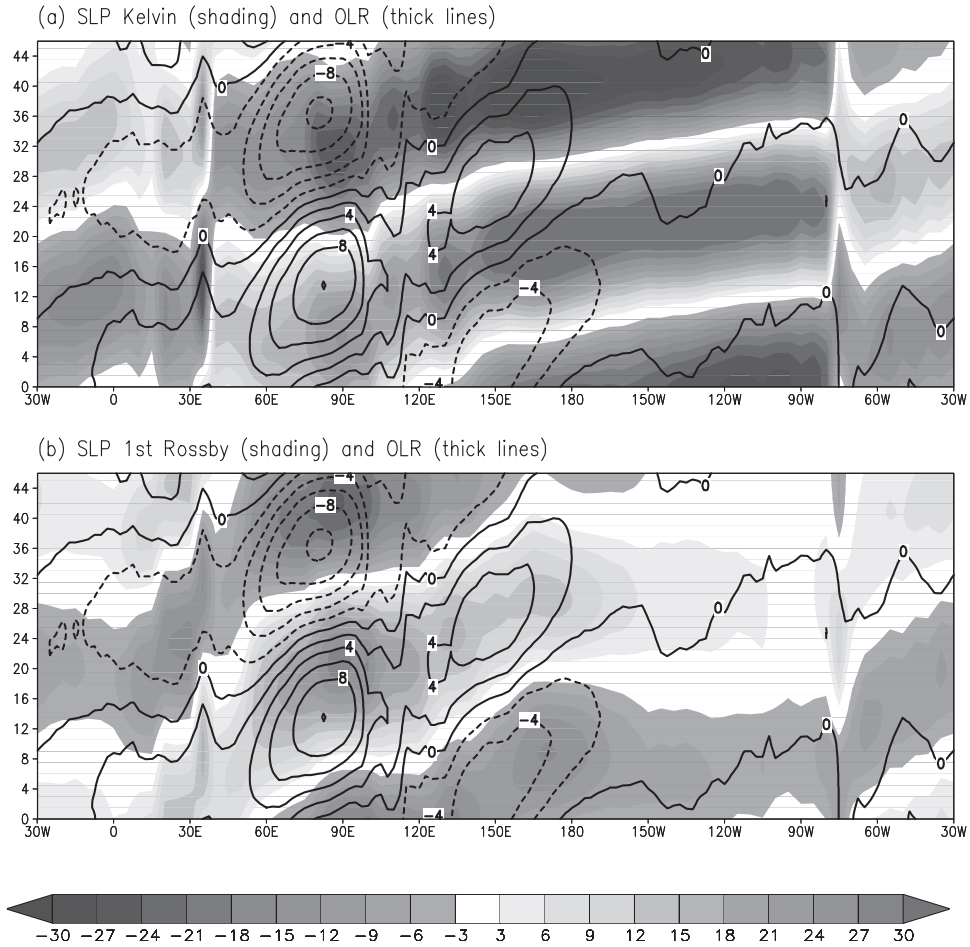

Figure 10. Hovmöller diagrams of (a) Kelvin waves of SLP (shading) and OLR (thick lines) anomalies, and (b) the first Rossby waves of SLP (shading) and OLR (thick lines) anomalies. SLP is in units of Pa. Contour interval of OLR anomalies is 2 Wm^{-2} with positive (negative) values being lightly (heavily) shaded. All quantities are averaged between 5°S and 5°N. Note that the negative slope in Figure 10b represents the westward propagation of free Rossby waves.

1996], the NASA Water Vapor Project precipitable water [*Maloney and Hartmann*, 1998], and the composite plots of radiosonde soundings from the Comprehensive Aerological Reference Data Set [*Kemball-Cook and Weare*, 2001].

[43] The maximum specific humidity anomaly, which is located at 700 hPa, appears 1 week after the enhanced convection reaches its maximum. It is speculated that this results from evaporation accompanying the fallout of precipitation in the deep convection. Beneath the moist region in the lowest level, a dry anomaly begins to develop. This drying may be created by the tongue of the new eastward propagating portion of the Kelvin waves. The moistening in the boundary layer occurring prior to the development of an enhanced convection accompanies the low-level wind convergence by the Kelvin and Rossby waves, setting up a favorable environment for new convection.

5. Summary and Conclusions

[44] The propagation and initiation mechanisms of the MJO are investigated using a CSEOF technique, regression analysis, and a wave decomposition method. By solving a space-time covariance function for the 22-year period of OLR data, a clean cycle of the convective anomalies is extracted. To retrieve dynamically consistent fields, other variables are regressed onto the OLR variation in CSEOF space. The regressed SLP and surface wind are further decomposed into Kelvin and Rossby wave components according to their meridional structures.

[45] Over the Indian Ocean, two separate surface convergence regions emerge, and they are formed by the different components of wind convergence. One is located just east of the enhanced convection, and the other convergence region appears in the leading eastern edge of the enhanced convection. The former, which is mainly from zonal wind convergence, leads the eastward movement of the convection anomaly, whereas the latter, which is due to meridional wind convergence, helps induce a new convection cell and expand the convection anomaly to the east. This is the first observational evidence showing the formation of the two different regions of surface convergence ahead of MJO convection by different wind components as previously identified in the SST-coupled GCM simulations by *Waliser et al.* [1999]. Indeed, the frictional meridional convergence

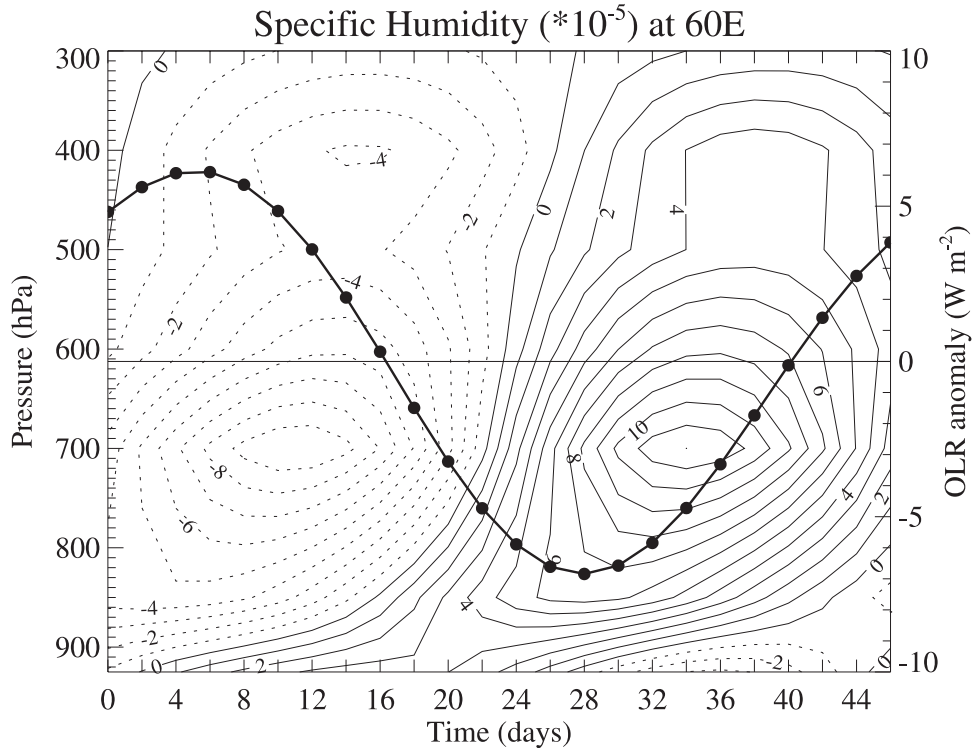

Figure 11. Time-pressure plot of specific humidity anomaly ($\times 10^{-5}$ kg kg^{-1}) at 60°E averaged from 5°S to 5°N. Thick line denotes corresponding OLR anomaly time series. The lowest level is 925 hPa.

in the boundary layer is regarded as a crucial maintenance mechanism for the MJO. The strong frictional convergence appears during the developing phase when the enhanced convection is located over the Indian Ocean and the Maritime Continents. After the convection core moves to the east of ~150°E, the convergence at the leading head of MJO convection disappears. The surface zonal wind convergence, however, seems to induce the eastward movement of the MJO convection core and both Kelvin and Rossby waves contribute to the formation of the downstream zonal convergence region. Considering that the divergence or convergence at the 850- and 200-hPa level is in phase with convection anomalies, the MJO can be simply characterized as the heat-induced large-scale circulation of the Matsuno-Gill type in the free troposphere and as frictional convergence in the boundary layer.

[46] At the western edges of the enhanced convection anomalies over the Indian Ocean, surface divergence appears due to both Kelvin and Rossby wave responses, suppressing the enhanced convection from the western edge. The divergence by the Kelvin component over the Indian Ocean is associated with Kelvin waves that have propagated from the region of reduced convection of the previous cycle over the Indian Ocean. The divergence by the Rossby component results from the decrease in strength of the westerly anomalies from the enhanced convection core to the upstream region.

[47] This interaction of Kelvin and Rossby waves is revealed to play an important role in initiating a new cycle of the MJO. That is, the circumnavigating Kelvin waves generated by the enhanced convection anomaly of the previous cycle over the Indian Ocean and the Rossby wave response to the reduced convection anomaly of the current cycle over the Indian Ocean appear to generate a new cycle of the MJO over the western Indian Ocean. Also, the life cycle of a convection anomaly interacts with that of the other convection anomaly through Kelvin and Rossby wave propagation. In this sense, the MJO may be considered as a self-generating and self-sustaining life cycle under its unique dipole structure over the warm-pool region.

[48] The current Kelvin and Rossby wave decomposition method produces reasonable patterns of Kelvin and Rossby wave propagation, although the governing equations (see Appendix D) involve some approximations. A noteworthy simplification is that the frictional damping coefficient is assumed to be identical to the radiational damping coefficient. In fact, the scales of length, time, and SLP change according to the ratio of these damping coefficients. Thus the structures of winds and SLP may vary depending on this ratio. As long as the ratio of frictional coefficient to radiational damping coefficient is not much greater than unity, Kelvin and Rossby structures may not vary significantly from the current case (where the ratio is 1). This method has often been employed in the study of oceanic variability associated with El Niño [e.g., *Delcroix et al.*, 1994; *Boulanger and Menkes*, 1995], and has provided an insightful picture of Kelvin and Rossby wave propagation associated with El Niño.

[49] This study, albeit imperfect, provides some insights into the propagation and onset mechanisms of the MJO. Numerical studies may render the relative importance among various factors including the effects of SST, latent heat flux and downward solar radiation and cloud longwave heating concerning the primary physical problems. As long

as idealized models or GCMs are dependent upon a parameterization for convection, however, a comprehensive assessment seems to remain difficult.

Appendix A: Nested Period

[50] The nested period, d, is chosen to be 48 days in this study. We view the MJO as an annually recurrent phenomenon. That is, space-time covariance statistics are assumed periodic with 1-year period. Since each year is 96 days in this study, we must assume a nested period to be an integer fraction of 96 days so that statistics are periodic each year. We stress that the choice of 40-day nested period is not acceptable in this particular case; statistics will not be periodic with 1-year period. If 1 year were 80 days, nested period would be 40 days.

[51] If one chooses a nested period of $2d$, then the spatial patterns similar to those shown in Figure 3 will repeat twice. Indeed, the nested period was initially assumed to be 96 days in the present study, for which the first two CSEOFs consists of two nearly identical sets of spatial patterns. If, on the other hand, one uses a nested period of $0.5d$, correct physical process will not be extracted, in general. In the present case, however, the physical process of interest is nearly of sinusoidal structure so that the second half of the process is a mirror image of the first half. Thus the first CSEOF would show half of the spatial patterns in Figure 3. Consequently, the corresponding PC time series must flip in sign every 24 days in order to describe the missing half of the spatial patterns in Figure 3. This oscillation of 24-day period in the PC time series does not represent purely stochastic component of variability but physical component of variability (i.e., ~48-day period of the MJO).

[52] The nested period chosen here may seem to be contradictory to the AR spectrum in Figure 1 (i.e., peak near 40 days). It should be noted, however, that the spectral peak is fairly wide and flat indicating variable nature of the MJO's period and phase. Thus, regardless of the nested period, as long as it is reasonable, the MJO physical process is split into at least two CSEOFs as described in Appendix B.

Appendix B: A Two-Mode Separation for Non-Phase-Locked Waves

[53] The present use of the CSEOF method is examined for the case in which the phase of the oscillation varies from one event to another. Under such a condition, the technique produces two evolution modes, which are temporally in a 90° out-of-phase relationship. The CSEOF analysis, however, extracts meaningful physical evolution patterns from the data. To demonstrate this, experimental tests have been carried out using simple artificial data as discussed below. First, let us consider a traveling disturbance in the form

$$D(\lambda,\varphi,t;k,\tau)=\cos(2\pi(k\lambda-t/\tau))\exp\left(-(\pi\varphi/20)^4\right),$$

$$\text{for } 35^\circ\text{E}<\lambda<155^\circ\text{W}, 10^\circ\text{S}<\varphi<10^\circ\text{N}, t=[1,500],$$

$$D(\lambda,\varphi,t;k,\tau)=0, \quad \text{otherwise}, \tag{B1}$$

where λ is longitude, φ is latitude, t is time, and k and τ are wave number and frequency, respectively. The data domain is ($\lambda \in [0, 360] \times \varphi \in [-20, 20]$). In the first experiment, artificial data, $T(\lambda, \varphi, t)$, were constructed as

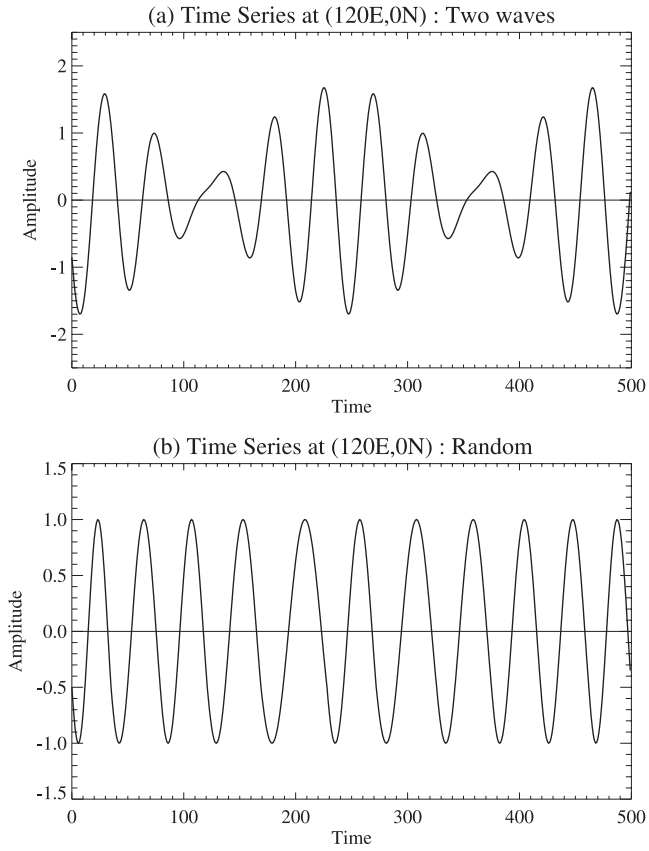

Figure B1. Time series of the artificial data (a) in equation (B2) and (b) in equation (B3) at (120°E, 0°N).

$$T(\lambda,\varphi,t)=D(\lambda,\varphi,t;k=2,\tau=48)$$
$$+0.71D(\lambda,\varphi,t;k=2,\tau=40). \tag{B2}$$

Thus the data consist of two traveling signals with different periods and henceforth different phase speeds. The time series at (120°E, 0°N) shows the modulation of the two traveling waves (Figure B1a). A CSEOF analysis on this data with a nested period of 48 results in two major modes, which together explain 99% of the total variability (Figure B2). As shown in the figure, the second mode is the 90° phase shift of the first mode. This second mode is produced because of the disturbances with a period different from the nested period. Note that the two modes together can reproduce the frequency modulation shown in Figure B1a as indicated by the combined variance. More general data are constructed by using three traveling patterns with three different periods, which also yields two main CSEOFs with the 90° phase relationship.

[54] The second experiment uses the following forcing function:

$$D(\lambda,\varphi,t;k,\tau)=\cos(2\pi(k\lambda-t/\tau_{\text{random}}))\exp\left(-(\pi\varphi/20)^4\right),$$

$$\text{for } 35^\circ\text{E}<\lambda<155^\circ\text{W}, 10^\circ\text{S}<\varphi<10^\circ\text{N}, t=[1,500], \tag{B3}$$

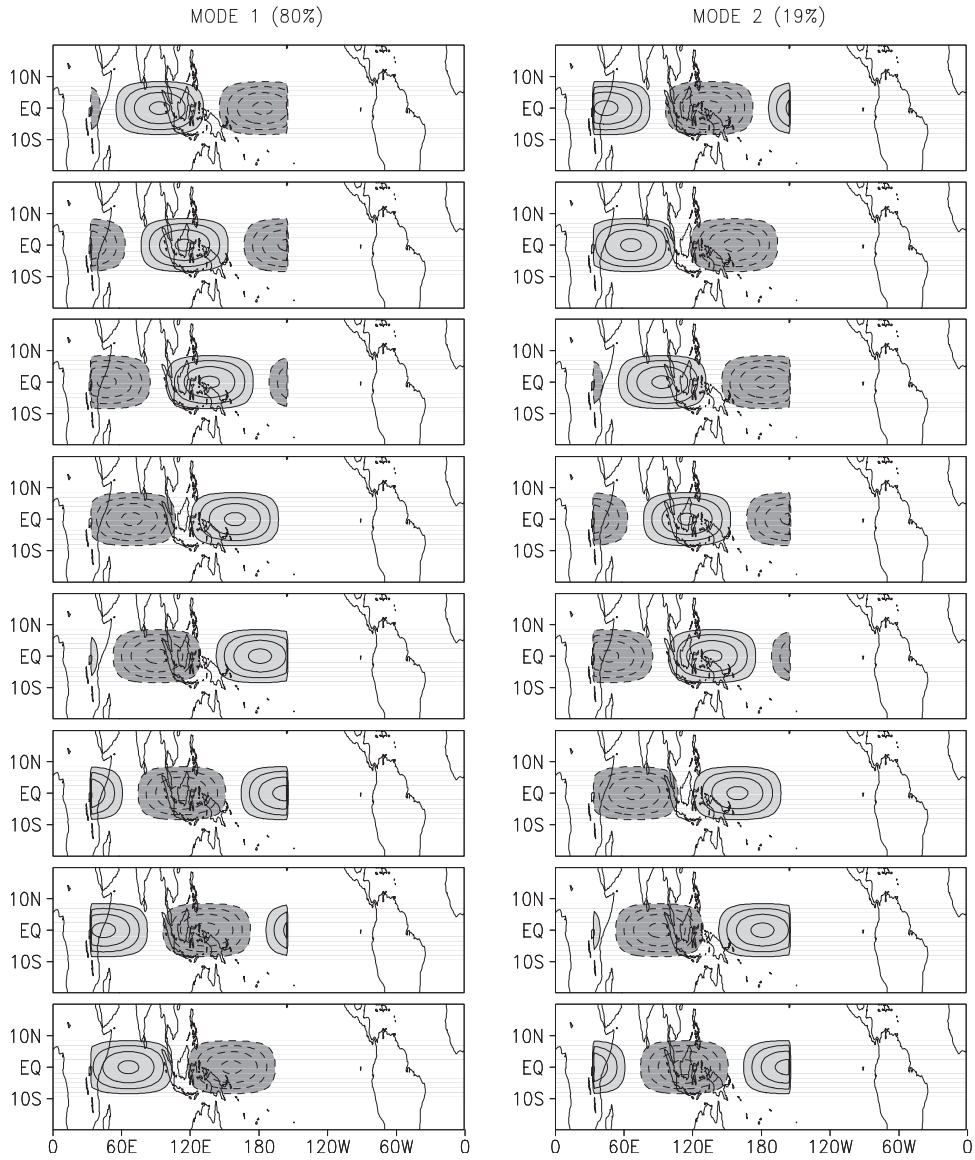

Figure B2. First and second CSEOFs of the artificial data in equation (B2).

where $\tau_{random} \sim N(48, 8)$ represents a random period with a Gaussian distribution with a mean of 48 and standard deviation of 8. The time series at (120°E, 0°N) shows the changing period of the disturbance (Figure B1b). The first two CSEOFs, which explain about 97% of total variability, are essentially the same as in Figure B2 and have the 90° phase difference. Again, the physical evolution structure was faithfully reproduced by the first mode or the second mode.

[55] Thus the limited experiments show that CSEOF analysis produces two modes that are 90° out of phase when the oscillation period of a physical process is not sharply defined. Indeed, this seems to be the case for the 30- to 60-day springtime or wintertime variability in the tropics. The physical evolution structure of the artificial data as seen in the first or the second CSEOF above appears to be accurate. It should also be mentioned that the interpretation of the resulting PC time series is not straightforward. A PC time series may not necessarily represent the amplitude of the corresponding mode; it includes the frequency modulation effect coming from a period-varying physical evolution.

Appendix C: Comparison With Extended EOFs and Complex EOFs

[56] Figures C1 and C2 show the first two extended EOFs of the same OLR data used in the present study. As can be seen, eastward propagation is apparent in both. While the spatial patterns of the first two extended EOFs provide similar statistical inferences to those of CSEOFs, the corresponding PC time series are very different from those of the CSEOFs (Figure C3). In extended EOF analysis, spatial patterns shown in Figures C1 and C2 are interpreted as time-lagged patterns in the data. Namely, the pattern labeled $t = 0$ is located at a specified time, then the pattern $t = -4$ is seen 4 days prior to the specified time and the pattern $t = +4$ is 4 days after the specified time and so

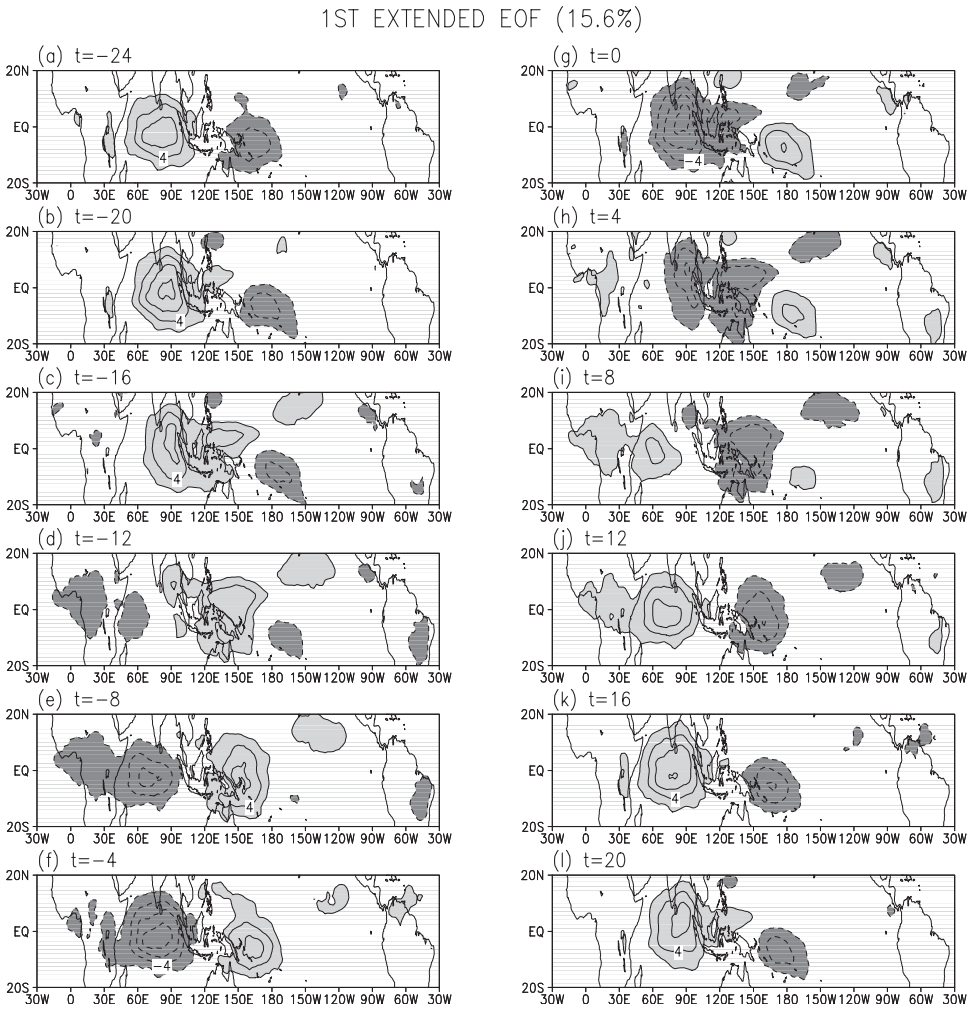

Figure C1. First extended EOF of the same filtered OLR data used for Figure 3.

forth. Whether one can see this pattern or not depends on the value of the corresponding PC time series at the specified time; this value determines the amplitude of the whole spatial patterns. The entire set of spatial patterns is translated to another time in the PC time series and is multiplied by the corresponding PC value; similar interpretation, then, is made as to the magnitude of these patterns in the data.

[57] With this in mind, the difference between CSEOF PC time series and extended EOF PC time series can be understood. Let us imagine a spatial point A (say, central Indian Ocean) where the time-lagged patterns in Figure C1 are observed. Then, in about 20 days, one expects similar time-lagged spatial patterns but with opposite sign. Thus the amplitude of PC time series should change sign in about 20 days. This sign change is clearly seen in the first two PC time series (Figure C3). Indeed, best AR spectrum of each time series shows a peak around the 40-day period (Figure C4). That is, this spectral peak is associated with a physical timescale rather than a stochastic timescale. In addition to this physical timescale, the extended EOF PC time series also show long-term undulation of the amplitude of spatial patterns shown in Figures C1 and C2.

[58] The CSEOF PC time series in Figure C3, on the other hand, contains only the stochastic component of variability aside from physical evolution shown in Figure 3. Note that each point of the PC time series is associated with only one snapshot in Figure 3; CSEOF patterns in Figure 3 are periodically extended in time to cover the entire data period.

[59] There are two related issues revolving around this difference. (1) While the spatial patterns in Figure C1 show eastward propagation of OLR anomalies (proper physical interpretation), the spatial patterns in Figure C1 do not actually move in time (computational interpretation). That is, computationally speaking, we see the $t = 0$ pattern at all time. This is misleading since, in fact, we see different spatial patterns in Figure C1 as time progresses. (2) Somehow, one interprets the corresponding PC time series as measuring the amplitude of the physical process (eastward propagation) shown in Figure C1. In a computational sense, however, the corresponding PC time series represents essentially the mean amplitude of the set of spatial patterns in Figure C1 with the $t = 0$ pattern centered at the specified time. Namely, the ~40-day oscillation in the extended EOF PC time series, in a sense, shows how the amplitude of the $t = 0$ spatial pattern changes in time. The $t = 0$ spatial

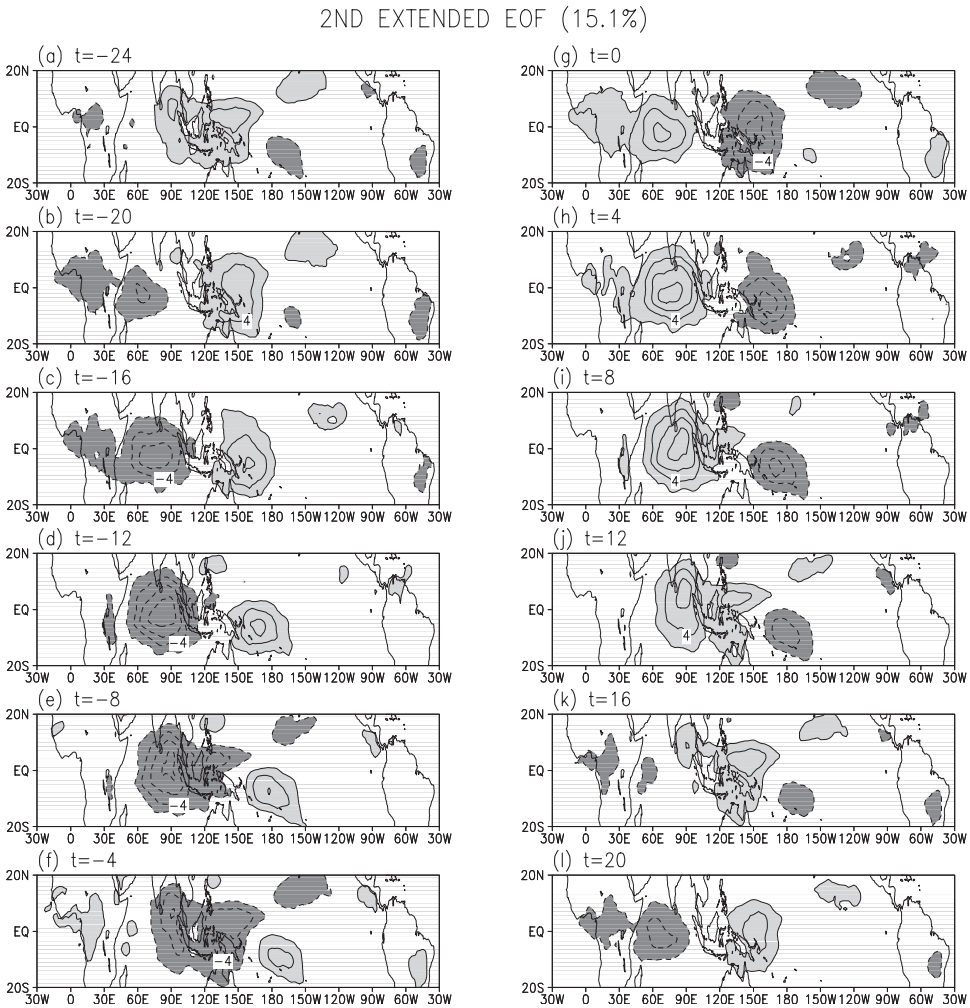

Figure C2. Second extended EOF of the same filtered OLR data used for Figure 3.

pattern, in reality, may just propagate eastward without changing its amplitude; then, in approximately 20 days, a similar spatial pattern of opposite sign may propagate into the same location from the west. In such a case, the amplitude of eastward propagation may not change, whereas the corresponding extended EOF PC time series would show a sinusoidal oscillation. Thus the extended EOF PC time series is contradictory to the physical interpretation (eastward propagation) of Figure C1.

[60] One might argue that spatial patterns in Figure C1, instead of being shifted by one time step each time, can be periodically extended in time. That is,

$$\begin{aligned} &A(t=-24)\ A(t=-20)\ldots\ A(t=0)\ldots\ A(t=20)\ A(t=24), \quad t=t,\\ &A(t=-20)A(t=-16)\ldots A(t=4)\ldots A(t=24)A(t=-24), \quad t=t+1,\\ &A(t=-16)A(t=-12)\ldots A(t=8)\ldots A(t=-24)A(t=-20), \quad t=t+2, \end{aligned} \tag{C1}$$

etc., where $A(t=t)$ is the spatial pattern in Figure C1 at time $t=t$. This may be a reasonable idea, but one has to know the periodicity of the particular physical process in order to extend the spatial patterns in a periodic manner. Further, one has to find when $A(t=0)$ pattern appears in the data in order to place the spatial patterns adequately in time.

[61] As in CSEOF analysis, the two extended EOFs are 90° out of phase with each other. The reason for this separation is different from that of CSEOF separation. With static spatial patterns shown in Figure C1, it is impossible to describe the movement of spatial patterns. The first extended EOF shows an OLR anomaly pattern extending from central Indian Ocean to the Maritime Continent ($t=0$ pattern). From a computational perspective, this is a stationary pattern; the anomaly pattern does not move but diminishes in amplitude and eventually reverses in sign in about 20 days. In order to describe the movement of spatial patterns, the second extended EOF chose the $t=10$ pattern in Figure C1 as its center spatial pattern (see Figures C1 and C2). Thus a numerical interpretation of the extended EOFs is

$$A(t=0) \Rightarrow B(t=0) \Rightarrow -A(t=0) \Rightarrow -B(t=0), \tag{C2}$$

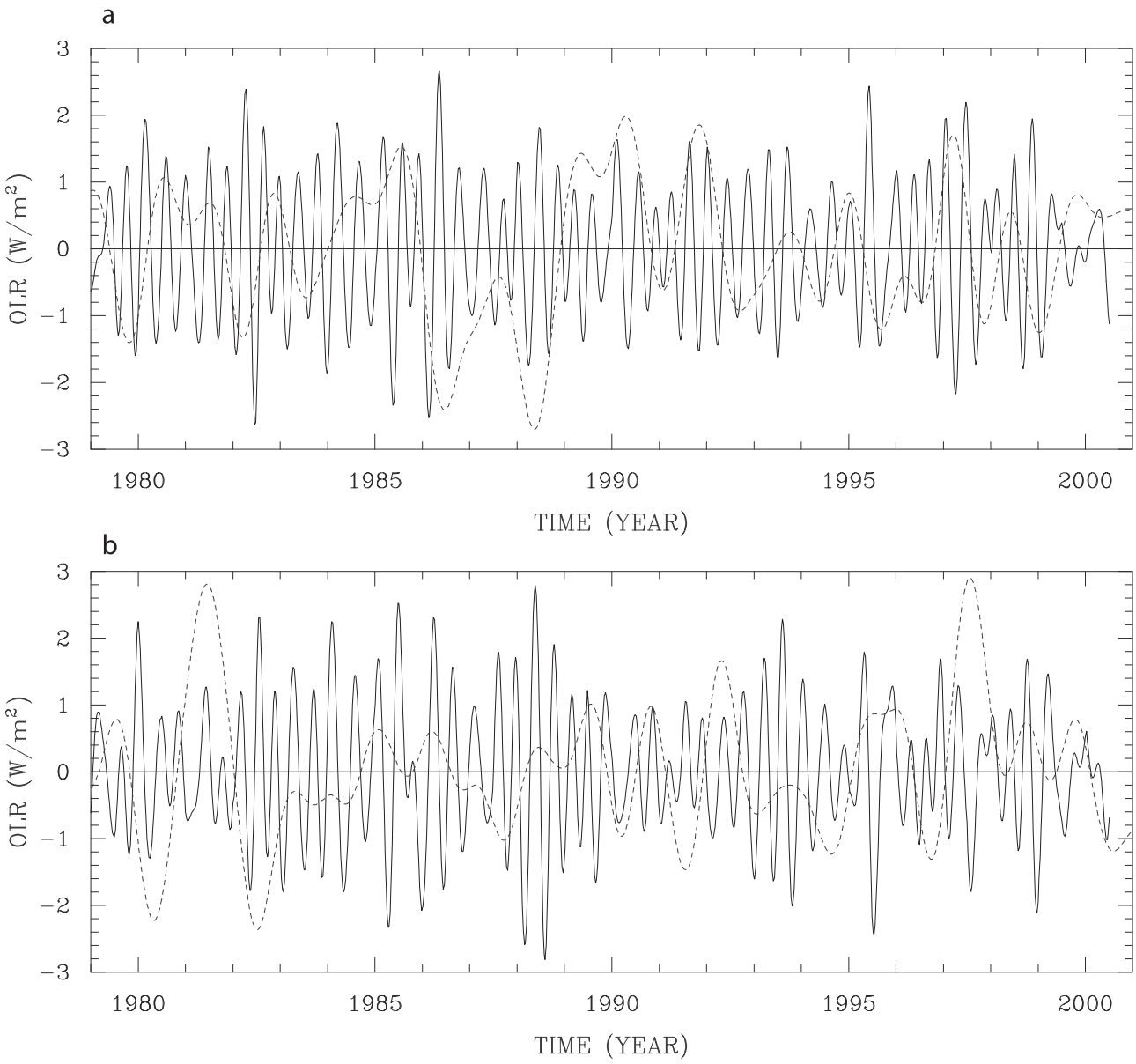

Figure C3. (a) First extended EOF PC time series (solid line) and the first CSEOF PC time series (dashed line), and (b) second extended EOF PC time series (solid line) and the second CSEOF PC time series (dashed line).

where $A(t = 0)$ is the $t = 0$ spatial pattern of the first extended EOF and $B(t = 0)$ is the $t = 0$ spatial pattern of the second extended EOF. This can be easily confirmed by calculating the cross-correlation between the two time series. Figure C5 shows that the two time series are maximally correlated at lag of ±10 days. It should also be mentioned that spatial patterns between $A(t = 0)$ and $B(t = 0)$ are often constructed by

$$C(t = t) = A(t = 0)\cos(2\pi\omega t) + B(t = 0)\sin(2\pi\omega t). \qquad \text{(C3)}$$

It is not necessarily true that $C(t = t)$ takes a form somewhere between $A(t = 0)$ and $B(t = 0)$.

[62] Finally, we would like to point out that the spectral peak in Figure C4 is rather broad, covering 30–50 days. This appears to indicate that the period of MJO (or the occurrence of MJO maximum phase) is somewhat variable. It is not clear in the observational data whether the broad peak is due to variable period of MJO or due to irregular occurrence of otherwise exactly periodic oscillation. In any case, MJO physical process is split into two CSEOFs with 90° phase relationship. No existing analysis technique is capable of precisely capturing such a variable phenomenon.

[63] Figure C6 shows the first complex EOF of the filtered OLR data. The real and imaginary spatial patterns in Figure C6 are indeed similar to the $t = 8$ spatial patterns of the first extended EOF and the second extended EOF, respectively. Further, PC time series are also highly correlated at $\rho = 0.7$ (figure not shown). In this special case of the MJO signal, which is nearly sinusoidal, complex EOF analysis does an excellent job in extracting the signal. The interpretation of the signal patterns is essentially the same as that of extended EOFs. Namely,

$$A(r) \Rightarrow B(r) \Rightarrow -A(r) \Rightarrow -B(r), \qquad \text{(C4)}$$

where $A(r)$ is real pattern and $B(r)$ is imaginary pattern. From a computational perspective, however, $A(r)$ and $B(r)$ are stationary patterns and corresponding PC time series

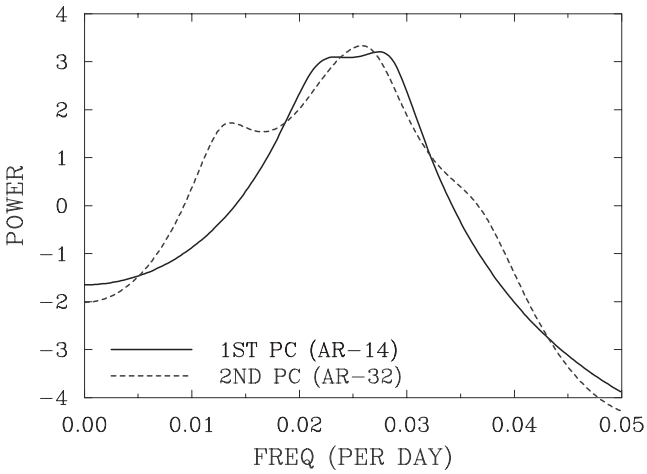

Figure C4. Best AR spectra of the first two extended EOF PC time series in Figure C3.

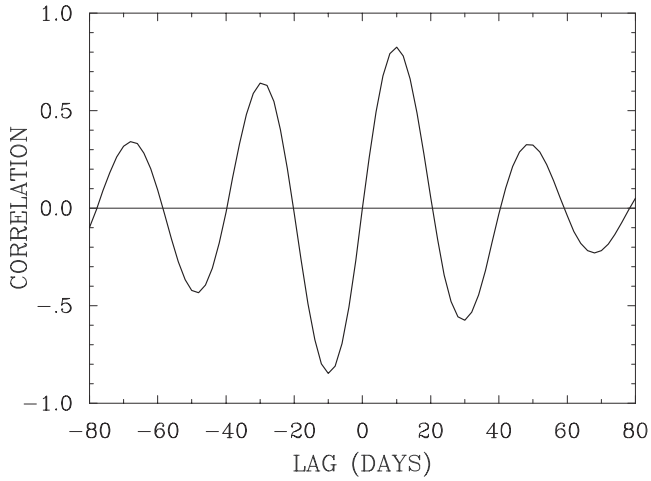

Figure C5. Cross-correlogram of the first two extended EOF PC time series.

represent the respective amplitude of these patterns. According to the PC time series, the real pattern $A(r)$ diminishes in amplitude and reverses its sign as time progresses. In a similar way, the imaginary pattern $B(r)$ stays at the same location while its amplitude changes in time. As in the case of extended EOFs, complex EOFs also suffer from the inconsistency of physical interpretation (eastward propagation in this specific example) and computational interpretation. While one is tempted to interpret Figure C6 as an eastward propagation of OLR anomaly, the corresponding PC time series treat these patterns as standing but oscillation patterns. According to the cross-correlogram of the real part and imaginary part of the PC time series, the oscillation period is approximately 40 days (not shown).

Appendix D: Kelvin and Rossby Decomposition

[64] Let us consider a system of nondimensionalized equations,

$$Ku - yv + \frac{\partial \phi}{\partial x} = 0, \qquad yu + \frac{\partial \phi}{\partial y} = 0, \qquad K\phi + \frac{\partial u}{\partial x} + \frac{\partial v}{\partial y} = F, \qquad \text{(D1)}$$

where K is a damping coefficient representing Rayleigh damping or Newtonian cooling, and F is a heating function. The solution is sought in the form

$$u(x,y,t) = q_0(x,t)u_0(y) + \sum_{m=1}^{\infty} q_m(x,t)u_m(y),$$

$$v(x,y,t) = \sum_{m=0}^{\infty} v_m(x,t)\Psi_m(y),$$

$$\phi(x,y,t) = q_0(x,t)\phi_0(y) + \sum_{m=1}^{\infty} q_m(x,t)\phi_m(y), \qquad \text{(D2)}$$

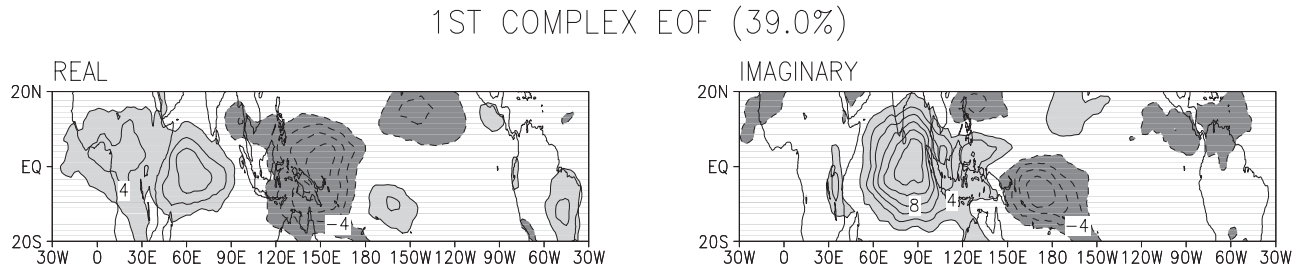

Figure C6. First complex EOF of the same filtered OLR data used for Figure 3.

where

$$u_0(y) = \phi_0(y) = \frac{1}{2}\Psi_0(y),$$

$$u_n(y) = \sqrt{\frac{n(n+1)}{2n(2n+1)}}\left(\frac{\Psi_{n+1}(y)}{\sqrt{n+1}} - \frac{\Psi_{n-1}(y)}{\sqrt{n}}\right),$$

$$\phi_n(y) = \sqrt{\frac{n(n+1)}{2n(2n+1)}}\left(\frac{\Psi_{n+1}(y)}{\sqrt{n+1}} + \frac{\Psi_{n-1}(y)}{\sqrt{n}}\right), \qquad \text{(D3)}$$

and $\Psi_n(y)$ are normalized Hermite functions. Note that solutions are given, after a long and tedious derivation, by

$$K\, q_0 + \frac{\partial q_0}{\partial x} = F_0,$$

$$K\, q_n - \frac{\partial q_n}{\partial x} = F_n, \qquad n = 1, 2, \ldots, \qquad \text{(D4)}$$

where

$$F_0(x,t) = \int_{-\infty}^{\infty} F(x,y,t)\phi_0(y)dy$$

$$F_n(x,t) = \int_{-\infty}^{\infty} F(x,y,t)\phi_n(y)dy. \qquad \text{(D5)}$$

Thus, as shown in equation (D4), each component of forcing and response is nicely separated with the meridional structure given by equation (D3). The zeroth mode is called the Kelvin mode, the first mode is the first Rossby mode, the second mode is the second Rossby mode, and so forth.

[65] Once u and ϕ are determined from (D4), the v solution follows from either the first or the third equation of (D1). Specifically, v is given, after a long derivation, by

$$v_0 = -\frac{\sqrt{6}}{2}F_1$$

$$v_n = -\frac{2}{n}\sqrt{\frac{2n+1}{n(n+1)}}\left(Kq_n - \frac{\partial q_n}{\partial x}\right) + \frac{1}{n}\sqrt{\frac{2n-1}{n-1}}F_{n-1}, n = 1, 2, \ldots \qquad \text{(D6)}$$

Note that each component of $v(x, y, t)$ is also separated. Further, v_n is connected only with q_n in equation (D6).

[66] Since we do not have a specific form of forcing, equation (D4) or (D6) cannot actually be solved to determine q_n and v_n. Thus q_n is estimated from observational data by projecting observational data on a specific structure function. Further, v_n is obtained by solving the first equation of (D1) with the nth component of $u(x, y, t)$ and $\phi(x, y, t)$.

[67] **Acknowledgments.** The authors would like to thank Brian Mackey and S. Tallapragada and three anonymous reviewers for their valuable comments, which helped to improve the paper. The OLR and NCEP/NCAR reanalysis data were provided by the NOAA-CIRES Climate Diagnostics Center from their web site at http://www.cdc.noaa.gov. This study was funded by the National Science Foundation (ATM-9613748) and the Department of Energy (DE-FG02-993462884).

References

Bladé, I., and D. Hartmann, Tropical intraseasonal oscillations in a simple nonlinear model, *J. Atmos. Sci.*, *50*, 2922–2939, 1993.

Boulanger, J.-P., and C. Menkes, Propagation and reflection of long equatorial waves in the Pacific Ocean during the 1992–1993 El Niño, *J. Geophys. Res.*, *100*, 25,041–25,059, 1995.

Chang, C.-P., Viscous internal gravity waves and low-frequency oscillations in the tropics, *J. Atmos. Sci.*, *34*, 901–910, 1977.

Chen, B., and M. Yanai, Comparison of the Madden-Julian oscillation (MJO) during the TOGA-COARE IOP with a 15-year climatology, *J. Geophys. Res.*, *105*, 2139–2149, 2000.

Chen, S., R. Houze, and B. Mapes, Multiscale variability of deep convection in relation to large-scale circulation in TOGA COARE, *J. Atmos. Sci.*, *53*, 1380–1409, 1996.

Chen, T.-C., and J.-M. Chen, On the relationship between the streamfunction and velocity potential of the Madden-Julian oscillation, *J. Atmos. Sci.*, *54*, 679–685, 1997.

Delcroix, T., J.-P. Boulanger, F. Masia, and C. Menkes, Geosat-derived sea level and surface current anomalies in the equatorial Pacific during 1986–1989 El Niño and La Niña, *J. Geophys. Res.*, *99*, 25,093–25,107, 1994.

Emanuel, K. A., An air-sea interaction model of intraseasonal oscillations in the tropics, *J. Atmos. Sci.*, *44*, 2324–2340, 1987.

Flatau, M., P. J. Flatau, P. Phoebus, and P. P. Niiler, The feedback between equatorial convection and local radiative and evaporative processes: The implications for intraseasonal oscillations, *J. Atmos. Sci.*, *54*, 2340–2373, 1997.

Gill, A. E., Some simple solutions for heat-induced tropical circulation, *Q. J. R. Meteorol. Soc.*, *106*, 447–462, 1980.

Hendon, H. H., A simple model of the 40–50 day oscillation, *J. Atmos. Sci.*, *45*, 569–584, 1988.

Hendon, H. H., Impact of air-sea coupling on the Madden-Julian oscillation in a general circulation model, *J. Atmos. Sci.*, *57*, 3939–3952, 2000.

Hendon, H. H., and B. Liebmann, The intraseasonal (30–50 day) oscillation of the Australian summer monsoon, *J. Atmos. Sci.*, *47*, 2909–2923, 1990.

Hendon, H. H., and M. L. Salby, The life cycle of the Madden-Julian oscillation, *J. Atmos. Sci.*, *51*, 2225–2237, 1994.

Hendon, H. H., and M. L. Salby, Planetary-scale circulations forced by intraseasonal variations of observed convection, *J. Atmos. Sci.*, *51*, 2225–2237, 1996.

Hsu, H.-H., Global view of the intraseasonal oscillation during northern winter, *J. Clim.*, *9*, 2386–2406, 1996.

Hsu, H.-H., B. J. Hoskins, and F.-F. Jin, The 1985/1986 intraseasonal oscillation and the role of the extratropics, *J. Atmos. Sci.*, *47*, 823–839, 1990.

Jones, C., and B. C. Weare, The role of low-level moisture convergence and ocean latent heat fluxes in the Madden and Julian oscillation: An obser-

vational analysis using ISCCP data and ECMWF analyses, *J. Clim.*, *9*, 3086–3104, 1996.
Kalnay, E., et al., The NCEP/NCAR 40-year reanalysis project, *Bull. Am. Meteorol. Soc.*, *77*, 437–471, 1996.
Kemball-Cook, S., and B. Wang, Equatorial waves and air-sea interaction in the boreal summer intraseasonal oscillation, *J. Clim.*, *14*, 2923–2942, 2001.
Kemball-Cook, S., and B. C. Weare, The onset of convection in the Madden-Julian oscillation, *J. Clim.*, *14*, 780–793, 2001.
Kemball-Cook, S., B. Wang, and X. Fu, Simulation of the intraseasonal oscillation in the ECHAM-4 model: The impact of coupling with an ocean model, *J. Atmos. Sci.*, *59*, 1433–1453, 2002.
Kim, K.-Y., and G. R. North, EOFs of harmonizable cyclostationary processes, *J. Atmos. Sci.*, *54*, 2416–2427, 1997.
Kim, K.-Y., G. R. North, and J. Huang, EOFs of one-dimensional cyclostationary time series: Computations, examples, and stochastic modeling, *J. Atmos. Sci.*, *53*, 1007–1017, 1996.
Lau, N.-C., and K.-M. Lau, The structure and propagation of intraseasonal oscillations appearing in a GFDL general circulation model, *J. Atmos. Sci.*, *43*, 2023–2047, 1986.
Lau, K.-M., and L. Peng, Origin of low-frequency (intraseasonal) oscillations in the tropical atmosphere: I. Basic theory, *J. Atmos. Sci.*, *44*, 950–972, 1987.
Lau, K.-M., L. Peng, C. H. Sui, and T. Nakazawa, Dynamics of super cloud clusters, westerly wind bursts, 30–60 day oscillations and ENSO: A unified view, *J. Meteorol. Soc. Jpn.*, *67*, 205–219, 1989.
Liebmann, B., and C. A. Smith, Description of a complete (interpolated) OLR dataset, *Bull. Am. Meteorol. Soc.*, *77*, 1275–1277, 1996.
Lin, J. W.-B., J. D. Neelin, and N. Zeng, Maintenance of tropical intraseasonal variability: Impact of evaporation-wind feedback and midlatitude storms, *J. Atmos. Sci.*, *57*, 2793–2823, 2000.
Madden, R. A., and P. R. Julian, Description of a 40–50 day oscillation in the zonal wind in the tropical Pacific, *J. Atmos. Sci.*, *29*, 1109–1123, 1972.
Madden, R. A., and P. R. Julian, Observations of the 40–50-day tropical oscillation-A review, *Mon. Weather Rev.*, *122*, 814–837, 1994.
Maloney, E. D., and D. L. Hartmann, Frictional moisture convergence in a composite life cycle of the Madden-Julian oscillation, *J. Clim.*, *11*, 2387–2403, 1998.
Matthews, A. J., Propagation mechanisms for Madden-Julian oscillation, *Q. J. R. Meteorol. Soc.*, *126*, 2637–2651, 2000.
Matthews, A. J., and G. N. Kiladis, The tropical-extratropical interaction between high-frequency transients and the Madden-Julian oscillation, *Mon. Weather Rev.*, *127*, 661–677, 1999.
Matthews, A. J., J. M. Slingo, B. J. Hoskins, and P. M. Inness, Fast and slow Kelvin waves in the Madden-Julian oscillation of a GCM, *Q. J. R. Meteorol. Soc.*, *125*, 1473–1498, 1999.
Neelin, J. D., I. M. Held, and K. H. Cook, Evaporation-wind feedback and low-frequency variability in the tropical atmosphere, *J. Atmos. Sci.*, *44*, 2341–2348, 1987.
Newton, H. J., *TIMESLAB*: *A Time Series Analysis Laboratory*, 623 pp., Wadsworth, Belmont, Calif., 1988.
Press, W. H., S. A. Teukolsky, W. T. Vetterling, and B. P. Flannery, *Numerical Recipes in FORTRAN: The Art of Scientific Computing*, 2nd ed., pp. 51–63, Cambridge Univ. Press, New York, 1992.
Salby, M. L., R. R. Garcia, and H. H. Hendon, Planetary-scale circulations in the presence of climatological and wave-induced heating, *J. Atmos. Sci.*, *51*, 2344–2367, 1994.
Shinoda, T., H. H. Hendon, and J. Glick, Intraseasonal variability of surface fluxes and sea surface temperature in the tropical western pacific and Indian oceans, *J. Clim.*, *11*, 1685–1702, 1998.
Slingo, J. M., Extratropical forcing of tropical convection in a northern winter simulation with the UGAMP GCM, *Q. J. R. Meteorol. Soc.*, *124*, 27–51, 1998.
Slingo, J. M., et al., Intraseasonal oscillations in 15 atmospheric general circulation models: results from an AMIP diagnostic subproject, *Clim. Dyn.*, *12*, 325–357, 1996.
Sperber, K. R., J. M. Slingo, P. M. Inness, and W. K.-M. Lau, On the maintenance and initiation of the intraseasonal oscillation in the NCEP/NCAR reanalysis and in the GLA and UKMO AMIP simulations, *Clim. Dyn.*, *13*, 769–795, 1997.
Waliser, D. E., K. M. Lau, and J.-H. Kim, The influence of coupled sea surface temperatures on the Madden-Julian oscillation: A model perturbation experiment, *J. Atmos. Sci.*, *56*, 333–358, 1999.
Wang, B., and T. Li, Convective interaction with boundary-layer dynamics in the development of a tropical intraseasonal system, *J. Atmos. Sci.*, *51*, 1386–1400, 1994.
Wang, B., and H. Rui, Dynamics of the coupled moist Kelvin-Rossby wave on an equatorial β-plane, *J. Atmos. Sci.*, *47*, 397–413, 1990.
Wang, B., and X. Xie, Coupled modes of the warm pool climate system: I. The role of air-sea interaction in maintaining Madden-Julian oscillation, *J. Clim.*, *11*, 2116–2135, 1998.
Woolnough, S. J., J. M. Slingo, and B. J. Hoskins, The relationship between convection and sea surface temperature on intraseasonal timescales, *J. Clim.*, *13*, 2086–2104, 2000.
Woolnough, S. J., J. M. Slingo, and B. J. Hoskins, The organization of tropical convection by intraseasonal sea surface temperature anomalies, *Q. J. R. Meteorol. Soc.*, *127*, 887–907, 2001.
Yanai, M., B. Chen, and W.-W. Tung, The Madden-Julian oscillation observed during the TOGA COARE IOP: Global view, *J. Atmos. Sci.*, *57*, 2374–2396, 2000.
Zhang, C., Atmospheric intraseasonal variability at the surface in the tropical western Pacific Ocean, *J. Atmos. Sci.*, *53*, 731–752, 1996.
Zhang, C., and H. H. Hendon, Propagating and standing components of the intraseasonal oscillation in tropical convection, *J. Atmos. Sci.*, *54*, 741–752, 1997.

K.-Y. Kim, Department of Meteorology, Florida State University, 404 Love Building, Tallahassee, FL 32306, USA. (kkim@met.fsu.edu)
K.-H. Seo, Climate Prediction Center, NOAA/NCEP, Camp Springs, MD 20746, USA. (kyong-hwan.seo@noaa.gov)